NCHRP 12-68

FY 2004

Rotational Limits for Elastomeric Bearings

Final Report

APPENDIX F

John F. Stanton

Charles W. Roeder

Peter Mackenzie-Helnwein

Department of Civil and Environmental Engineering

University of Washington

Seattle, WA 98195-2700

TABLE OF CONTENTS

LIST OF FIGURES

LIST OF TABLES

APPENDIX F Development of Design Procedures.

This appendix describes the development of design procedures. That subject requires discussion of five primary topics, each of which is treated in a separate subsection. The focus is on shear strains caused by the various loadings, because they are the critical quantity that determines whether debonding occurs.

Section F.1 addresses shear strain demand, and in particular it describes the relationships between external loads and internal shear strains.

Section F.2 addresses shear strain capacity. Two models are developed from the test results, and they link the amplitude of the total shear strain to the level of debonding damage. This is done for both monotonic and cyclic loading.

Section F.3 addresses loading demand. The forces and rotations that the bearing experiences must be known in order to determine the shear strains that they cause. These forces and rotations should be evaluated for each bridge during its design, but estimates of them are obtained in this section from typical bridge geometries and loadings to guide the development of the proposed bearing design specifications..

Section F.4 details the evaluation of the two different models for shear strain capacity, and Section F.5 describes the process of developing detailed design provisions from the foregoing sections. Section F.6 contains a summary of the findings of the appendix.

F.1 Derivation of Shear Strains in the Elastomer.

Determination of strains in the elastomer is complicated, because the material is nearly incompressible, is nonlinear, and experiences very large strains. An accurate evaluation is possible only with Finite Element Analysis, as described in Appendix E, and even then it presents significant challenges. A simpler, albeit approximate, approach to analysis is needed for design.

Gent and Lindley (e.g. Gent and Lindley, 1959a, Gent and Meinecke, 1970, Lindley and Teo, 1978) pioneered the analysis of laminated bearings and developed and presented a linearized analysis procedure. Conversy (1967) extended it to allow for finite values of the bulk modulus, and Stanton and Lund (2004) provided numerical values of all the necessary coefficients, for different bulk modulus values. That approach forms the basis of the procedure used for the design method used in this research, and is summarized here. It is approximate, because it assumes a parabolic distribution of displacement through the thickness of the elastomer, but, as the Finite Element Analyses show, that approximation proves to be remarkably good, and, for the geometries and stresses used in practical bearings, the errors are small compared with those arising from other sources, such as characterization of material properties. Its simplicity compared with any other alternatives makes it an attractive choice.

Two types of behavior must be distinguished. The first is defined here as “uplift” an refers to any situation in which the loading surface (i.e. the sole plate between the girder and bearing) remains in full contact with the bearing at all times. This always occurs when the bearing has bonded external plates. It may also occur in the absence of bonded external plates if the compression is large enough to prevent any separation. The most

important consequence is that hydrostatic tension stress may be induced in the elastomer if the rotation demand is large relative to the bearing's rotation capacity.

In the second type of behavior, referred to here as "lift-off", the rotation is large enough that the loading surface separates from the bearing over part of its area. By definition this can only occur in the absence of bonded external plates.

From an analytical viewpoint, the first behavior involves constant boundary conditions, while in the second the boundary (i.e. the region in contact with the loading surface) changes with the loading. Those latter conditions constitute a contact problem, for which analysis is much more complex. The two types of behavior are addressed in Sections F.1.1 and F.1.2.

F.1.1 Response without Lift-off

F.1.1.1 Internal Stresses

The internal stresses in the elastomer are developed here. They demonstrate fundamental behavioral properties of the bearing and are used in subsequent sections.

The analysis is based on the following assumptions:

- The rubber is perfectly bonded to the steel plates.
- The steel plates are rigid in both axial tension and flexure.
- No edge cover exists.
- The rubber bulges laterally in a parabolic shape.

In the linear theory developed by Gent and Lindley (1959a) the internal stress state can be shown to consist of two sets of stresses superimposed on each other. The displacement fields that correspond to them are shown for a single bonded layer in Figure F.1.

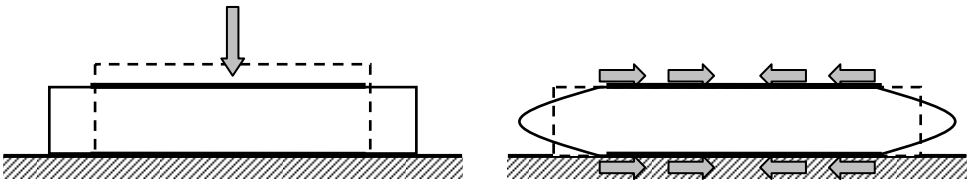

Figure F.1. Displacement Fields for Component Loadcases.

In the first loadcase, the elastomer is treated as being perfectly debonded from the steel plates above and below it. Under pure axial load, it shortens vertically and spreads laterally, without any resistance from the steel plates, due to the Poisson effect. For this loading, as for all loadings, Poisson's ratio, ν, is very nearly equal to 0.5 because the elastomer is almost incompressible.

The stresses and strains are described in a set of Cartesian coordinates, in which *z* is vertical, *x* is horizontal and parallel to the bridge axis and *y* is horizontal in the transverse direction. The vertical stress and the local shear strain at the edge are given by

$$\sigma_{zz} = E\varepsilon_{zz} \tag{F-1}$$

$$\gamma_{xz} = 0 \tag{F-2}$$

Here, positive stress and strain are tensile. In the second loadcase, the vertical displacement is held constant, and horizontal stresses are applied to the top and bottom surfaces of the elastomer, which are pulled inwards to their original horizontal positions. The nearly-constant volume property causes the layer to bulge at the mid-thickness as its top and bottom surfaces are pulled inwards. For this loadcase, the vertical stress and the shear strain are controlled (Stanton and Lund, 2004) by

$$\frac{t^2 K}{12G}\nabla^2\sigma_{zz} - \sigma_{zz} = -K\varepsilon_{zz} \tag{F-3}$$

$$\frac{d\sigma_{xx}}{dx} + \frac{d\tau_{zx}}{dz} = 0 \tag{F-4}$$

where

G = shear modulus of the elastomer

K = bulk modulus of the elastomer

ε_{zz} = vertical strain

σ_{zz} = vertical direct stress

σ_{xx} = horizontal direct stress

τ_{zx} = shear stress

In Gent's theory, the stress at a point is also assumed to be hydrostatic, so σ_{xx} , σ_{yy} and σ_{zz} are all equal. For the general case of a bearing whose plan shape is a rectangle of arbitrary aspect ratio, the problem is 3-D and closed form solutions are not available. The equations may be solved using a series solution (e.g. Conversy 1967) or by numerical integration (e.g. Stanton and Lund 2004). 3-D Finite Element analysis is also a challenge because the nonlinearity of the problem requires an iterative solution, and, given the mesh refinement needed, the computational demands become enormous. However, for an infinite strip, the analysis becomes 2-D, and closed form solutions are possible. Furthermore, Finite Element Analysis of the 2-D system is computationally feasible, and may be used to explore behavior and to verify the simpler linear theory. The primary results for an infinite strip are presented here.

Equation (F-3) may be simplified by using the Compressibility Index, λ, developed by Stanton and Lund

$$\lambda = S\sqrt{\frac{3G}{K}} \tag{F-5}$$

where S = Shape Factor $= \dfrac{\textit{loaded plan area}}{\textit{perimeter area free to bulge}} = \dfrac{LW}{2t(L+W)}$ (F-6)

In Equation (F-6), L is the bearing length, W is the width and t is the elastomer layer thickness. The Compressibility Index indicates the extent to which bulk compressibility of the elastomer affects the response, and arises naturally in the development of the equations.

It is also convenient to define the dimensionless coordinate, $\xi = \dfrac{2x}{L}$, where the origin is at the center of the bearing. Thus $\xi = \pm 1$ correspond to the edges. Then Equation (F-3) becomes, for a 2-D system in the x-z plane,

$$\frac{1}{\lambda^2}\frac{d^2\sigma_{zz}(\xi)}{d\xi^2} - \sigma_{zz}(\xi) = -K\varepsilon_{zz}(\xi) \tag{F-7}$$

For pure axial loading, the vertical strain, $\varepsilon_{zz}(\xi)$, is constant across the cross-section and therefore independent of ξ, so the vertical stress is obtained by taking $\varepsilon_{zz}(\xi)$ as a constant value, ε_a, in Equation (F-7), which can be solved to give

$$\sigma_{zz}(\xi) = K\varepsilon_a\left[1 - \frac{\cosh(2\lambda\xi)}{\cosh(2\lambda)}\right] \tag{F-8}$$

The shear strain at the top or bottom surface of the layer is then

$$\gamma_{zx}(\xi) = -6S\varepsilon_a\left[\frac{\sinh(2\lambda\xi)}{2\lambda\cosh(2\lambda)}\right] \tag{F-9}$$

These solutions are for the general case of a slightly compressible material, for which the compressibility is defined by λ. For a completely incompressible material, $\lambda = 0$, and the equations become indeterminate. Equations (F-8) and (F-9) can be solved by using binomial expansion, and the equations reduce to

$$\sigma_{zz}(\xi) = 2S^2E\varepsilon_a\left(1 - \xi^2\right) \tag{F-10}$$

and

$$\gamma_{xz}(\xi) = 6S\varepsilon_a\xi \tag{F-11}$$

The distribution of stress in the elastomer under compressive load is illustrated on the right side of Figure F.2.

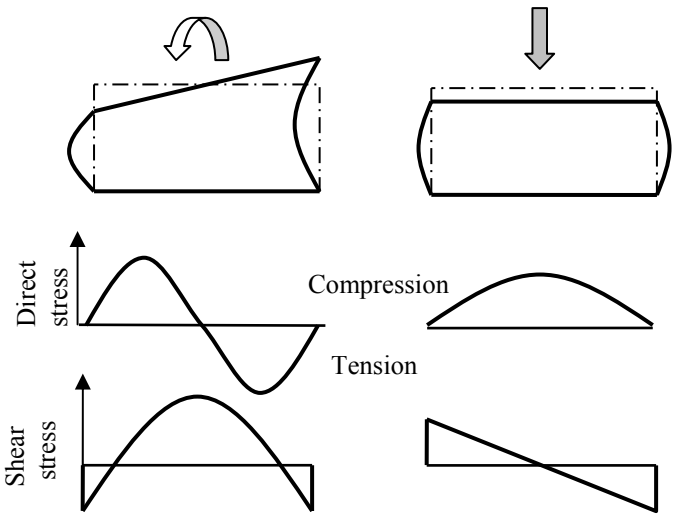

Figure F.2. Stresses in the Elastomer due to Rotation and Compression Load.

For pure rotation, the vertical strain is distributed linearly across the bearing surface, i.e.

$$\varepsilon_{zz}(\xi) = x\frac{\theta_L}{t} = S\theta_L\xi \tag{F-12}$$

where θ_L = the rotation per layer of the bearing. For the general, compressible, case the vertical stress is derived from Equation (F-7) as

$$\sigma_{zz}(\xi) = KS\theta_L\left[\xi - \frac{\sinh(2\lambda\xi)}{\sinh(2\lambda)}\right] \tag{F-13}$$

$$\gamma_{zx}(\xi) = -6\frac{S^2}{(2\lambda)^2}\theta_L\left[1 - \frac{2\lambda\cosh(2\lambda\xi)}{\sinh(2\lambda)}\right] \tag{F-14}$$

These may also be simplified for the special case of complete incompressibility ($\lambda = 0$), to give

$$\sigma_{zz}(\xi) = \frac{2}{3}ES^3\theta_L\left(\xi - \xi^3\right) \tag{F-15}$$

and

$$\gamma_{zx}(\xi) = S^2 \theta_L \left(1 - 3\xi^2\right) \tag{F-16}$$

The distribution of stress in the elastomer due to rotation is illustrated in Figure F.2. These equations are used in Sections F.1.1.2 and F.1.1.3 to define the two most important bearing properties: stiffness and peak shear strain.

F.1.1.2 Bearing Stiffnesses

The bearing stiffnesses in response to axial load and rotation are needed for analysis. The axial stiffness is needed for computing the axial deflection, which is in turn needed for evaluation of hydrostatic tension. The rotational stiffness is used for checking stability of the bearing, for verifying lateral-torsional buckling of the girder (Mast 1993) and, if the bearing is equipped with a slider, for determining whether the stainless steel will lift off from the PTFE. In most cases, under-estimating the stiffness leads to a safe prediction (i.e. it is a conservative choice). The major exception is hydrostatic tension, for which a low estimate of stiffness is likely to lead to an unsafe prediction of stress (i.e. internal fracture will be predicted not to occur when if fact it will).

Stanton and Lund (2004) show that these responses can be expressed in terms of the shape factor, S, of the bearing layer. The axial and rotational stiffnesses of one layer are:

$$K_a = \frac{P}{\Delta_a} = \frac{EA\left(A_a + B_a S^2\right)}{t} \tag{F-17}$$

$$K_r = \frac{M}{\theta_L} = \frac{EI}{t}\left(A_r + B_r S^2\right) \tag{F-18}$$

where

S = shape factor

M = moment

E = Young's modulus ($\approx 3G$)

A_a, B_a, A_r, B_y = dimensionless constants

Δ_a = axial displacement

θ_L = rotation angle applied to each layer of the bearing.

For common S values (4 to 8), the A_a and A_r terms are small compared with the $B_a S^2$ and $B_r S^2$ terms and may be ignored in the interests of simplicity, with little error. Their values are given by Gent and Lindley as $A_a = A_r = 1.0$ for rectangular shapes, and 1.333 for an infinite strip. Values for B_a and B_r are given in Figure F.3 and Figure F.4, taken from Stanton and Lund (2004). They are functions of L/W, and λ, the Compressibility Index. The axial stiffness coefficient, B_a, is shown only up to $L/W = 1.0$. For larger values of L/W, B_a can be found by interchanging L and W.

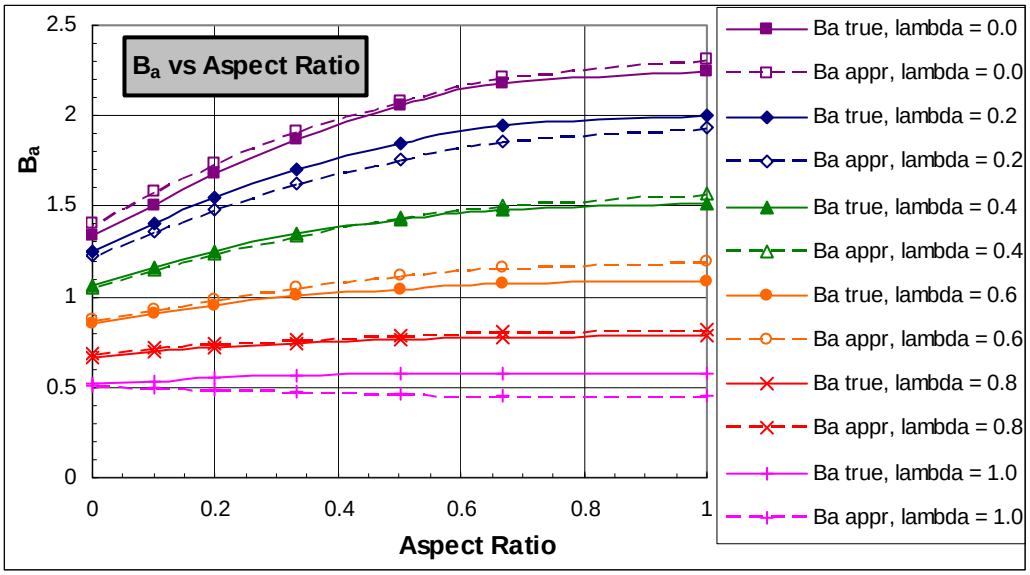

Figure F.3. Stiffness Coefficient B_a (from Stanton and Lund).

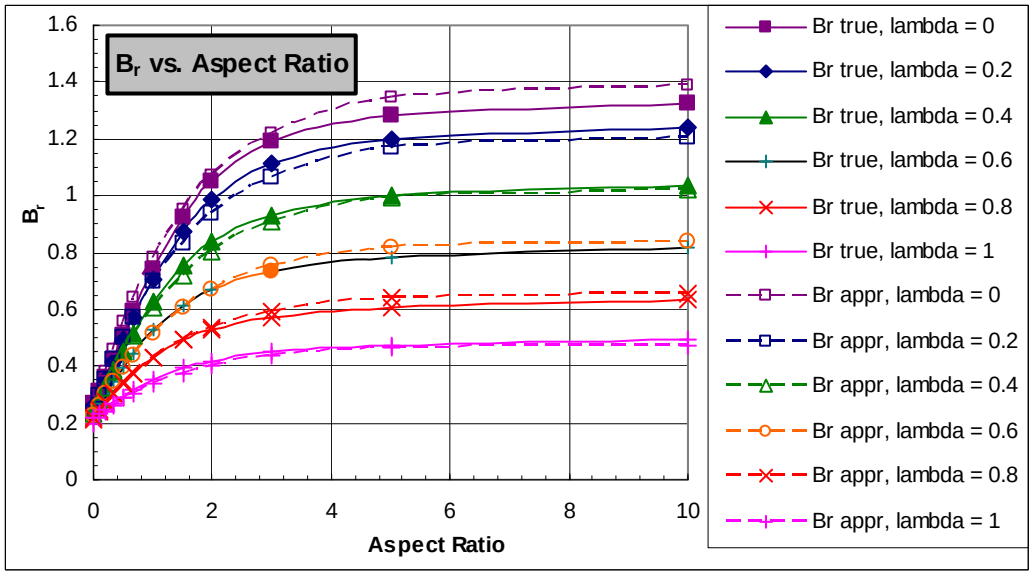

Figure F.4. Stiffness Coefficient B_r (from Stanton and Lund).

Empirical approximations for these quantities in rectangular bearings, intended for use in the range $0 < \lambda < 1.0$, are:

$$B_a \approx (2.31 - 1.86\lambda) + (-0.90 + 0.96\lambda)(1 - \min\{L/W, W/L\})^2 \quad \text{(F-19)}$$

$$B_r \approx (0.24 - 0.024\lambda) + (1.15 - 0.89\lambda)(1 - \exp(-0.64L/W)) \quad \text{(F-20)}$$

In figures F-3 and F-4, the true values are shown as solid lines with solid symbols, and the empirical approximations are shown as dashed lines and open symbols.

For circular bearings, Gent and Meinecke (1970) give B_a = 2.0 and B_r = 2/3 for the incompressible case. By using the approximation proposed for compression by Gent and Lindley (1959a), the effective modulus of elasticity may be expressed as

$$\frac{1}{E_{eff}} \approx \frac{1}{EB_aS^2} + \frac{1}{K} \quad \text{(F-21)}$$

from which the stiffness coefficient B_a for the compressible case becomes

$$B_a \approx \frac{2}{1 + 2\lambda^2} \quad \text{(F-22)}$$

Similarly, for rotation,

$$B_r \approx \frac{1}{1.5 + \lambda^2} \quad \text{(F-23)}$$

For most elastomers used in bridge bearings, $K \approx 450{,}000$ psi, and $G \approx 110$ psi so, for S = 6, $\lambda \approx 0.167$ and the values of parameters such as B_a differ little from those of a completely incompressible material, for which $\lambda = 0.0$.

Because in this approach the problem is characterized as linear, superposition is valid and the solutions from different load-cases, such as compression and rotation, can be added directly. This greatly simplifies the calculations.

F.1.1.3 Maximum Shear Strain

The maximum shear strain in the elastomer is of interest because it is often used as a design criterion. It can be obtained from Equation (F-4). The results are, for axial load and rotation respectively,

$$\gamma_a = (C_aS)\varepsilon_a \quad \text{(F-24)}$$

$$\gamma_r = (C_rS)\frac{L}{2t}\theta_L \quad \text{(F-25)}$$

where

C_a, C_r = dimensionless constants

γ_a= maximum shear strain caused by axial load

γ_r = maximum shear strain caused by rotation

Equations (F-17) and (F-24) may also be combined to give the shear strain due to axial load directly in terms of the stress. This may be done most simply by ignoring the A_a term in Equation (F-17), on the basis that it is much smaller than the $B_a S^2$ term. Then

$$\gamma_a = C_a S \varepsilon_a \approx C_a S \frac{\sigma_a}{3GB_a S^2} = D_a \frac{\sigma_a}{GS} \tag{F-26}$$

where

$$D_a = \frac{C_a}{3B_a} \tag{F-27}$$

Similarly, the shear strain caused by rotation may be expressed in terms of the *L/t* ratio alone (and not the shape factor) as

$$\gamma_r = D_r \left(\frac{L}{t} \right)^2 \theta_L \tag{F-28}$$

where

$$D_r = \frac{C_r}{4(1 + L/W)} \tag{F-29}$$

For typical bearings, S is about 6, B_a is about 2, and A_a is 1.0, and the error resulting from ignoring the A_a and A_r terms is approximately 1.5%. Values for C_a, D_a, C_r and D_r are shown in Figure F.5 through Figure F.8. Empirical approximations for the shear strain coefficients, valid in the range $0 < \lambda \leq 1.0$, are

$$C_a \approx \left(8.6 - 4.8(0.667 - L/W)^2\right) * \left(1 - 0.75\lambda + 0.124\lambda^2\right) \tag{F-30}$$

$$C_r \approx \min\left\{\left(2 - \lambda^2\right)\left(1 + L/W + 0.66\lambda^2\right), \left(4.8 - 2.25\lambda\right)\right\} \tag{F-31}$$

$$D_a \approx \max\left\{d_{a1}, \left(d_{a2} + d_{a2} * L/W\right)\right\} \tag{F-32}$$

where

$$d_{a1} = 1.06 + \lambda * (0.210 + \lambda * 0.413)$$

$$d_{a2} = 1.506 + \lambda * (-0.071 + \lambda * 0.406)$$

$$d_{a3} = -0.315 + \lambda * (0.195 + \lambda * (-0.047))$$

$$D_r \approx \min\left\{ \frac{1.552 - 0.627\lambda}{2.233 + 0.156\lambda + L/W},\ 0.5 \right\} \qquad \text{(F-33)}$$

In Figure F.5 through Figure F.8, the true values are shown as solid lines with solid symbols, and the empirical approximations are shown as dashed lines and open symbols. The value of D_a remains essentially constant for $L/W > 3$.

To minimize possible confusion over the value S of W and L, a convention is needed. The one used here is that W is always the length of the side parallel to the axis of rotation under consideration. This holds true for computing both stiffness and shear strain coefficients. Usually, the bearing will experience rotation about its weak axis, so W will be the length of the long side and L, the length of the short side. Thus, for a 10 in. x 20 in. bearing, L = 10 in. and W = 20 in. for bending about the weak axis, but L = 20 in. and W = 10 in. for bending about the strong axis. The coefficients D_a and D_r given in Equations (F-32) and (F-33) compute the shear strain on the side of the bearing, of length W, that is the one parallel to the axis of rotation. Because both strains occur in the same place, they are additive.

Note that, under axial load alone, the largest shear strain occurs on the long side of the bearing. For the common case of rotation about the weak axis, the largest shear strains due to both axial and rotation loading individually occur in the same place, so shear strains need only be calculated there. If the primary loading is about the strong axis, the largest total shear strain may occur either at the long side (due to axial load alone) or at the short side (due to axial plus rotation effects). Both must be calculated, and the larger controls.

For a circular bearing,

D_a and D_r may be approximated as

$$D_a = 1.0 \qquad \text{(F-34)}$$

$$D_r = 0.375 \qquad \text{(F-35)}$$

The values for D_a and D_r in Equations (F-34) and are derived from Gent and Meinecke (1970). They are also consistent with the equations in the existing AASHTO LRFD Design Specifications. They are lower than the values for rectangular bearings, thereby demonstrating that, for the same rotation or average axial stress, the circular bearing will experience lower shear strain.

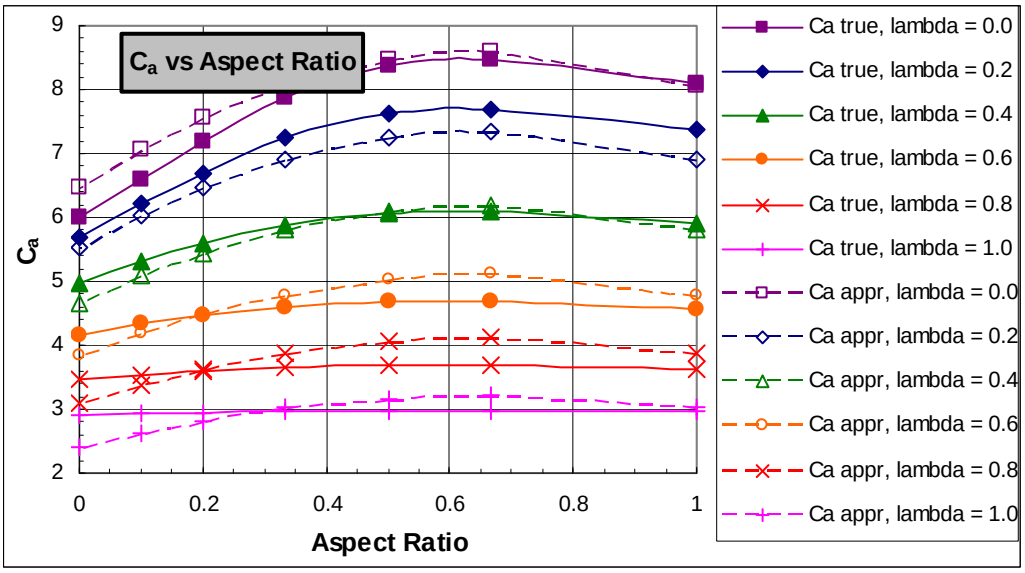

Figure F.5. Shear Strain Coefficient C_a.

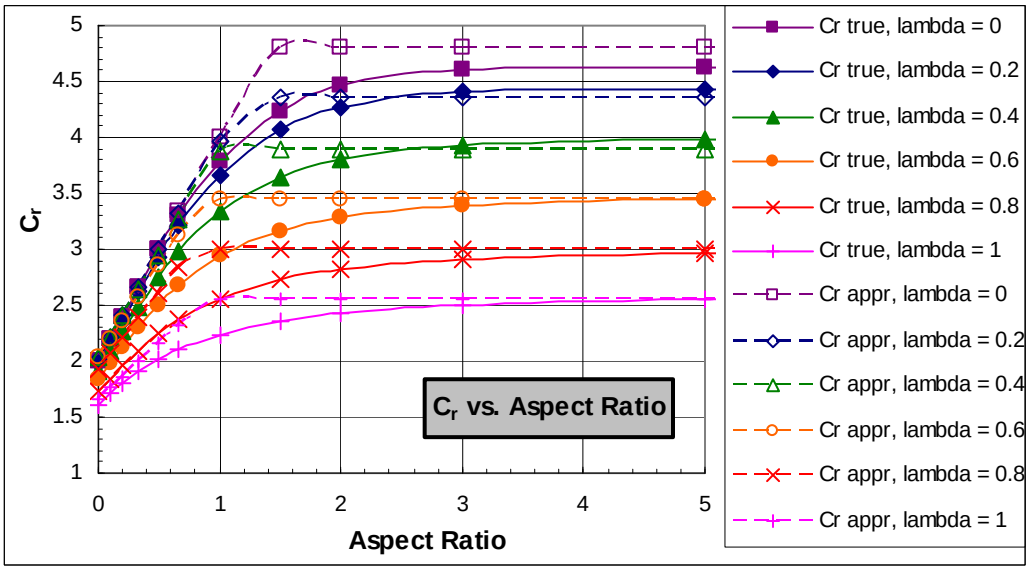

Figure F.6. Shear Strain Coefficient C_r.

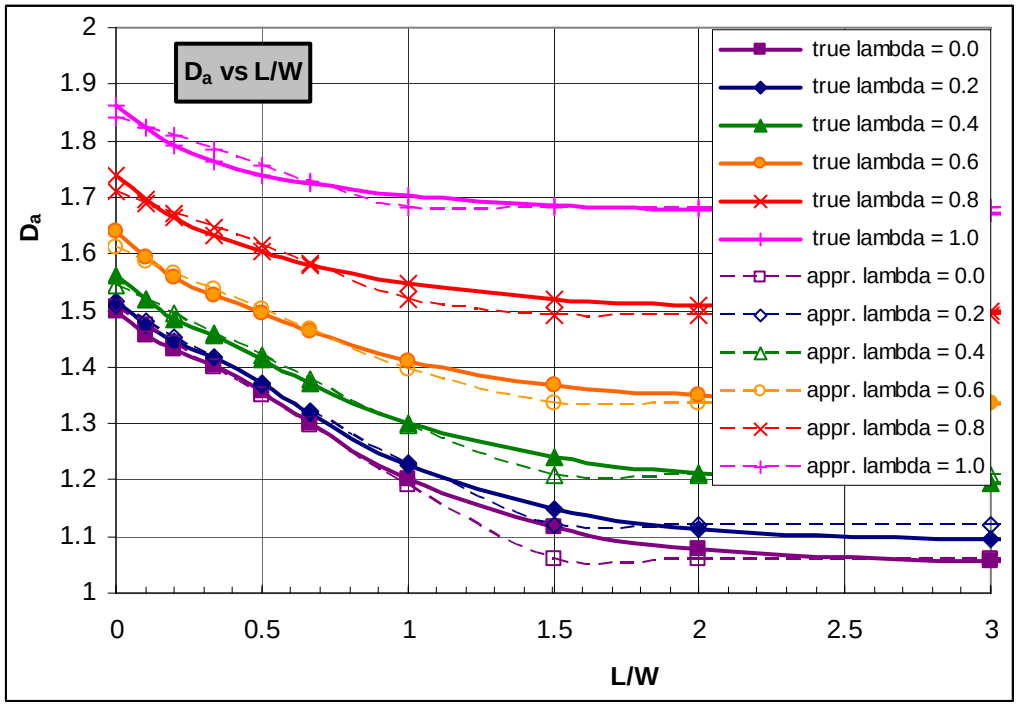

Figure F.7. Shear Strain Coefficient D_a.

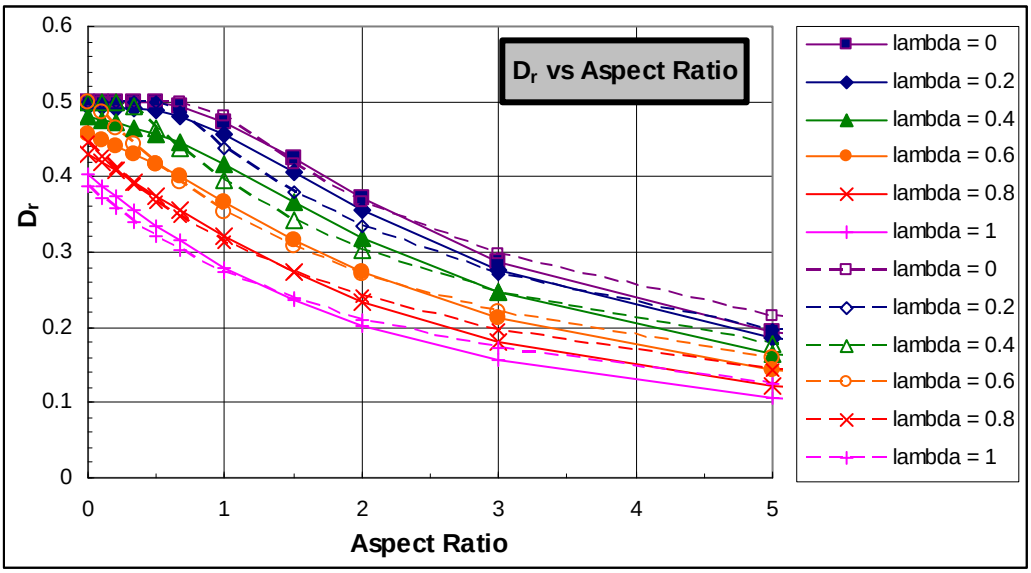

Figure F.8. Shear Strain Coefficient D_r.

Example.

Consider a bearing with four internal layers each 20” x 10” x ½” thick, made from rubber with G = 0.135 ksi, K = 450 ksi, and subjected to compressive load of 200 kips and a rotation of 0.01 radians about its weak axis.

The shape factor is

$$S = \frac{LW}{2t(L+W)} = \frac{10*20}{2*0.5*(10+20)} = 6.66$$

The compressibility index is

$$\lambda = S\sqrt{\frac{3G}{K}} = 6.666\sqrt{\frac{3*0.135}{450}} = 0.200$$

From Figure F.3 and Figure F.4, B_a = 1.85 and B_r = 0.50 (exact values), so the axial stiffness of the layer is

$$K_a = \frac{P}{\Delta} = \frac{EA(A_a + B_a S^2)}{t} = \frac{0.405*200(1+1.85*6.66^2)}{0.5} = 13480\ kip/in$$

The load of 200 kips causes an axial strain of

$$\varepsilon_a = \left(\frac{200kips}{13480kips/in}\right) \Big/ 0.5in = 0.0297in/in = 2.97\%$$

The rotational stiffness of the layer is

$$K_r = \frac{M}{\theta_L} = \frac{EI(A_r + B_r S^2)}{t} = \frac{0.405*16667(1+0.50*6.66^2)}{0.5} = 313{,}500\ in-kip/rad$$

so the rotation of θ_L = 0.01 rad/4 layers = 0.0025 rad/layer induces a moment of

$$M = 313{,}500*0.0025 = 784\ in-kips$$

For λ = 0.2 and $L/W = AR$ = 0.5, the coefficient values are C_a = 7.6 and C_r = 2.9. The peak shear strains due to combined axial force and rotation are:

$$\gamma_{a,\max} = C_a S \varepsilon_a = 7.6*6.66*0.0297 = 1.50$$

$$\gamma_{r,\max} = C_r S \frac{L}{2}\frac{\theta_L}{t} = 2.9*6.66*\frac{10}{2}*\frac{0.0025}{0.5} = 0.48$$

Note that, for these calculations, the gross dimensions of the bearings were used. This ignores the fact that the cover rubber behaves slightly differently than the rubber in the core of the bearing. The specifications proposed in Appendix G include a slight refinement of the definition that accounts approximately for the difference.

F.1.1.4 Combined Loading

A bearing subjected to combined compression and rotation may be analyzed using the linear theory outlined in Sections F.1.1.1 through F.1.1.3. There are two major questions of interest: whether a bearing without external plates experiences lift-off at the tension edge, and consequently higher shear strains on the compressive side, and whether a bearing with external bonded plates experiences internal hydrostatic tension.

Figure F.9 illustrates the development of hydrostatic tension. Note that the maximum hydrostatic tension typically does not occur at the edge. Recall that the linear theory

assumes that the direct stress at a point is the same in all directions, so it is also equal to the hydrostatic stress.

The total vertical stress in the elastomer is obtained for an infinite strip by adding Equations (F-8) and (F-13) and including the terms from the first loadcase. The result, given in Equation (F-36) is also written in terms of the coefficients A_a, etc., so that the equation may be extended for use with aspect ratios other than an infinite strip.

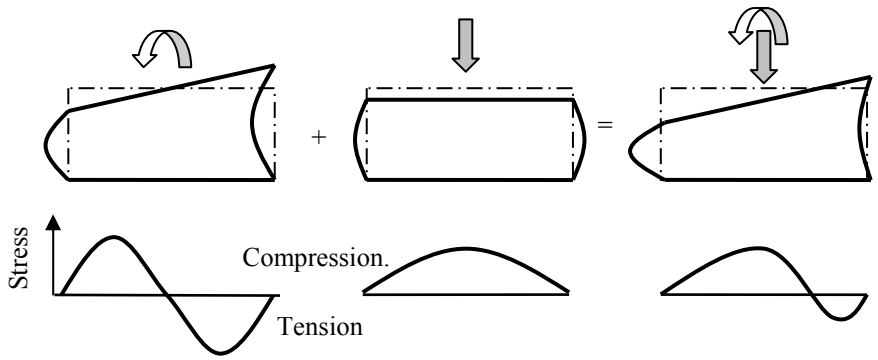

Figure F.9. Hydrostatic Tension under Combined Compression and Rotation.

$$\sigma_{zz}(\xi)=\left\{A_a E+\frac{3}{4}B_a K\left[1-\frac{\cosh(2\lambda\xi)}{\cosh(2\lambda)}\right]\right\}\varepsilon_a+\left\{A_r E\xi+3.75B_r K\left[\xi-\frac{\sinh(2\lambda\xi)}{\sinh(2\lambda)}\right]\right\}S\theta_L \tag{F-36}$$

The characteristics of the total response depend on the relative magnitudes of ε_a and $S\theta_L$, which represent the magnitudes of the individual loadings. For this purpose it is convenient to introduce the variable θ_c, defined as

$$\theta_c=-\frac{\varepsilon_a}{S} \tag{F-37}$$

The strain ε_a is negative for compression, in which case $\theta_c > 0$. Physically, θ_c represents the rotation at which the vertical displacement on the "tension" side of the bearing starts to become net upwards. It is called the characteristic rotation.

To find the location of the maximum vertical stress, Equation (F-36) must be differentiated and the result set to zero. Doing this and using the fact that

$$\cosh^2(2\lambda\xi)=\sinh^2(2\lambda\xi)+1 \tag{F-38}$$

leads to

$$\left[H_a^2 - H_r^2\right]\sinh^2(2\lambda\xi) + \left[-2F_r H_a\right]\sinh(2\lambda\xi) + \left[F_r^2 - H_r^2\right] = 0 \qquad \text{(F-39)}$$

Where

$$H_a = 0.75 B_a K \frac{\lambda}{\cosh(2\lambda)} \varepsilon_a \qquad \text{(F-40)}$$

$$H_r = 3.75 B_r K \frac{\lambda}{\sinh(2\lambda)} \theta_L S \qquad \text{(F-41)}$$

$$F_r = \left(EA_r + 3.75 K B_r\right)\theta_L S \qquad \text{(F-42)}$$

Equation (F-39) is a quadratic in $\sinh(2\lambda\xi)$, which can be solved in closed form. The value of ξ, the location of the peak hydrostatic stress, can be extracted from it and substituted back into Equation (F-36) to find the peak hydrostatic stress.

If ξ is less than 1.0, the maximum vertical stress occurs within the bearing and the elastomer experiences vertical tension and, by implication, hydrostatic tension. If $\xi >$ 1.0, the peak stress occurs outside the bearing, so the result is of no practical interest from the viewpoint of hydrostatic tension, since the vertical stress everywhere within the bearing is compressive.

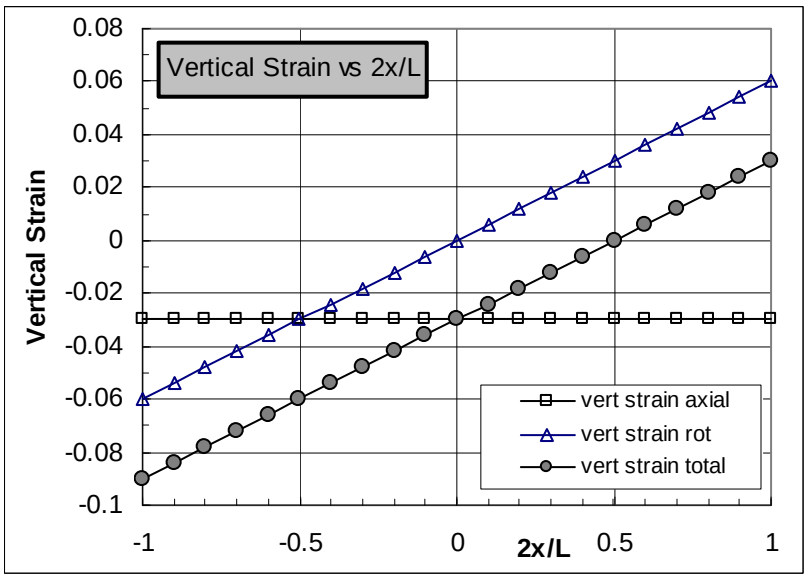

Figure F.10. Distribution of Vertical Strain across the Bearing.

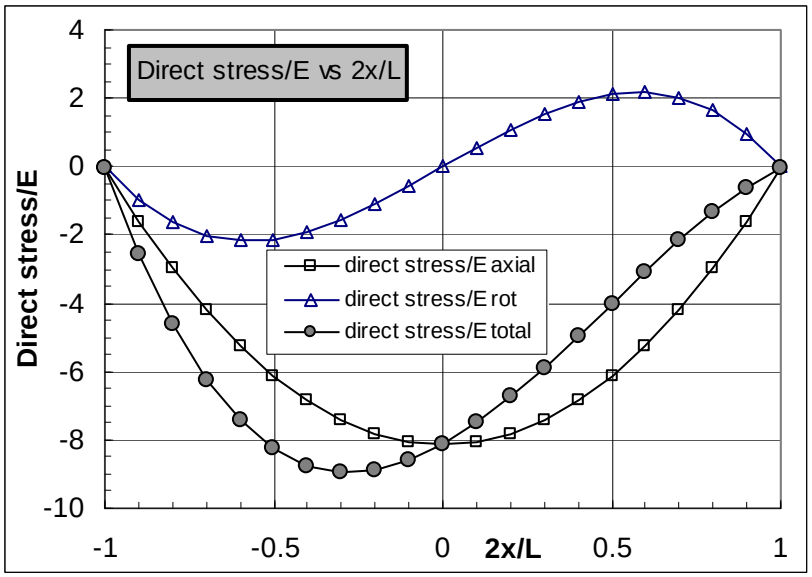

Figure F.11. Distribution of Vertical Stress across the Bearing.

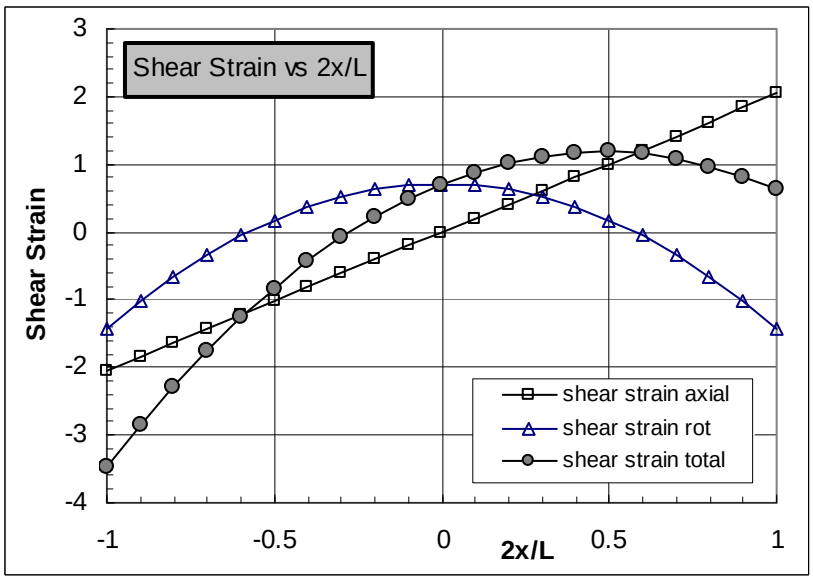

Figure F.12. Distribution of Shear Strain across the Bearing.

Figure F.10 through Figure F.12 show the vertical stress, the vertical strain and the shear strain across the elastomer layer for the case $\theta = 2\theta_c$. In the figures, negative stress and strain indicate compression. (ε_a = - 0.03 in/in was used in this case, but that fact does not affect the figures). For these conditions the "tension" side of the bearing experiences net upward displacement, or vertical tensile strain. However, the total vertical stress is everywhere compressive. This implies that the sole plate does not lift off from the elastomer layer.

The fact that vertical tension strain does not necessarily lead to vertical tension stress represents behavior that differs from that of conventional materials. It is explained by the

fact the elastomer's near incompressibility causes the material to shift laterally as well as vertically. Some rubber from the compressed side is indeed forced outwards into the bulge on that side. However, some of it is also pushed across the bearing to the tension side, where it occupies the space left by the upward movement of the top plate on that side. This behavior is confirmed by the fact that the signs of the shear strains at the two edges are opposite (see Figure F.12), showing that both faces are bulging outwards. If the "tension" face bulges outward, the hydrostatic stress just inside it must be compressive. That result is confirmed in Figure F.11.

It is shown in Section F.1.1.5 that, in the bearing with external plates, the hydrostatic stress first becomes tensile only when the rotation reaches a value of approximately $3\theta_c$. At that rotation, the shear strain on the tension faces changes sign, so the edge bulges inwards, confirming the existence of hydrostatic tension. Furthermore, in bearings with no external plates, lift-off also starts at a rotation of $\theta = 3\theta_c$, since the interface can carry no tension stress. Thus the tension side must rise due to rotation through three times the distance required to reach its original elevation, in order to cause shear strain reversal at the edge or hydrostatic tension in the interior of the elastomer.

F.1.1.5 Uplift and Hydrostatic Tension

If external plates are bonded to the bearing, rotation may cause hydrostatic tension in the interior of the rubber. Excessive hydrostatic tension may cause the rubber to rupture (Gent and Lindley, 1959b). A comprehensive analysis of the internal stresses is complex, because it must address both 3-D effects and finite compressibility. However, a simplified solution can be obtained by applying the linear theory to an infinite strip layer, as was done in Section F.1.1.4. An infinite strip allows the analysis to be 2-D, which simplifies the closed form analysis and also makes Finite Element Analysis feasible. The analysis described below is confirmed by the Finite Element studies described in Appendix E.

Equations (F-36) through (F-42) presented a way of finding the peak vertical stress in the elastomer, including the effects of material compressibility. However, the equations are a little complex. They can be simplified by specializing them for the geometry of the infinite strip and by assuming that the material is completely incompressible. Those assumptions reduce Equation (F-36) to

$$\sigma_{hyd}(\xi) = \frac{2}{3} E(\xi - 3\alpha)(1 - \xi^2) \qquad \text{(F-43)}$$

where $\xi = 2x/L$ is measured from the center of the bearing layer and

$$\alpha = -\frac{\varepsilon_a}{S\theta_L} = \frac{\theta_c}{\theta_L} \qquad \text{(F-44)}$$

Note that ε_a is negative for compressive strain at the center of the bearing, so in most cases, α will be positive. Equation (F-43) shows that the distribution of hydrostatic stress is governed by the single variable α. This observation simplifies the calculations significantly.

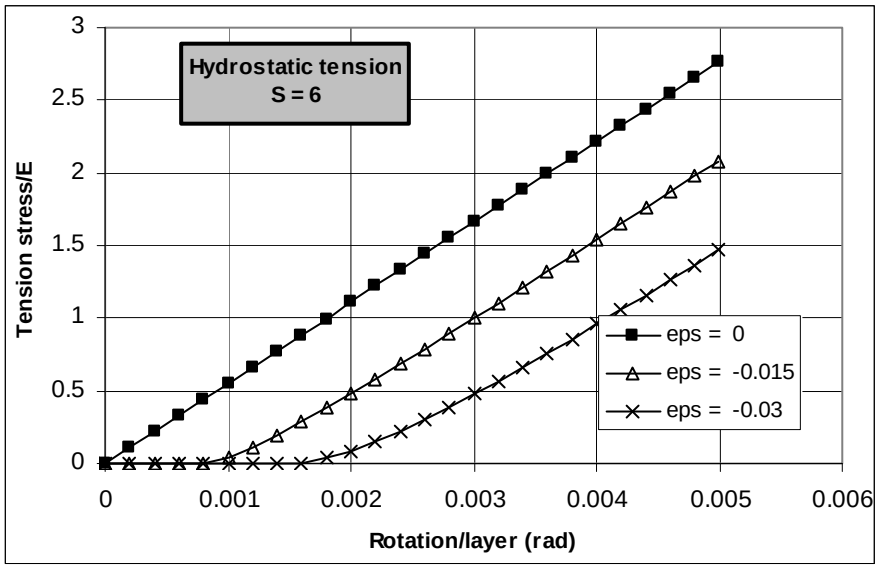

Figure F.13. Hydrostatic Tension vs. Rotation for Various Compression Strains. S = 6.

For specific bearings subjected to specific loadings, ε_a and θ_L, figures such as Figure F.13 can be prepared. It shows the peak tensile stress, normalized with respect to E, for various ε_a and θ_L values, for a bearing with $S = 6$ and incompressible material. Negative axial strain indicates compression. The lower regions of the curves for $\varepsilon_a \neq 0$ are curvilinear because the location of the peak hydrostatic stress moves inwards towards the center of the bearing as the rotation increases while the axial strain remains constant.

Figure F.13 shows the results for a single bearing, but results for a range of bearings can be shown on a single dimensionless plot. This is achieved by finding the location, ξ, of the maximum hydrostatic stress from Equation (F-43), and substituting back to find the peak stress. The value of ξ that maximizes $\sigma_{hyd}(\xi)$ is given by

$$\xi_{\max} = \alpha + \sqrt{\alpha^2 + \frac{1}{3}} \qquad \text{(F-45)}$$

If $\xi_{max} > 1$, the direct stress is compressive everywhere within the bearing and no hydrostatic tension exists. This is the case when $\alpha > 1/3$, which implies that the rotation per layer lies below $3\theta_c$.

For design, the problem is likely to be to determine the maximum hydrostatic tension stress, if any, that exists under a particular combination of axial load and rotation. It is obtained by using in Equation (F-43) the value of ξ found from Equation (F-45). The result, after normalization, is

$$\sigma_{hyd,norm} = \frac{\sigma_{hyd,\max}}{ES^3\theta_L} = f(\alpha) = \frac{4}{3}\left\{-\alpha\left(1-\alpha^2\right)+\left(\alpha^2+\frac{1}{3}\right)^{1.5}\right\} \qquad \text{(F-46)}$$

This representation is convenient because it allows all combinations of shape factor, axial strain and rotation to be shown on a single plot.

The constant of normalization in Equation (F-46) contains the term S^3 so, for a given α, the hydrostatic stress rises rapidly with increasing S. The configuration most likely to lead to problems with hydrostatic stress is therefore a bearing with external bonded plates, a high shape factor, light axial load, and large rotation. This combination of events may occur in steel bridges during construction. If bolting or welding the bearing to the girder really is essential for the service load condition, the possibility of temporary hydrostatic tension during construction may be avoided by leaving the bearings unattached until after the deck has been cast. By then, the initial rotation due to camber, and the potential for internal rupture in the bearing, will largely have been eliminated.

Similar calculations, but including compressibility, were conducted using Equations (F-36) through (F-43). The hydrostatic stress was again normalized using with respect to $ES^3\theta_L$. It was found that all bearings with a single value of λ, regardless of the individual values of S, E and K, all lay on a single curve. Curves for different λ values are shown in Figure F.14, with the approximate curve for complete incompressibility, marked "approx 0" and computed from Equation (F-46).

Common bearings have $S \approx 6$ and $\lambda \approx 0.2$. In that range, the approximate incompressible curve in Figure F.14 gives values that are very close to the exact ones. Given the other approximations in the calculations, it is proposed that Equation (F-46) be accepted as a satisfactory design equation for computing the peak hydrostatic tension stress, regardless of the compressibility of the elastomer. It was developed for an infinite strip, but is conservative for other geometries.

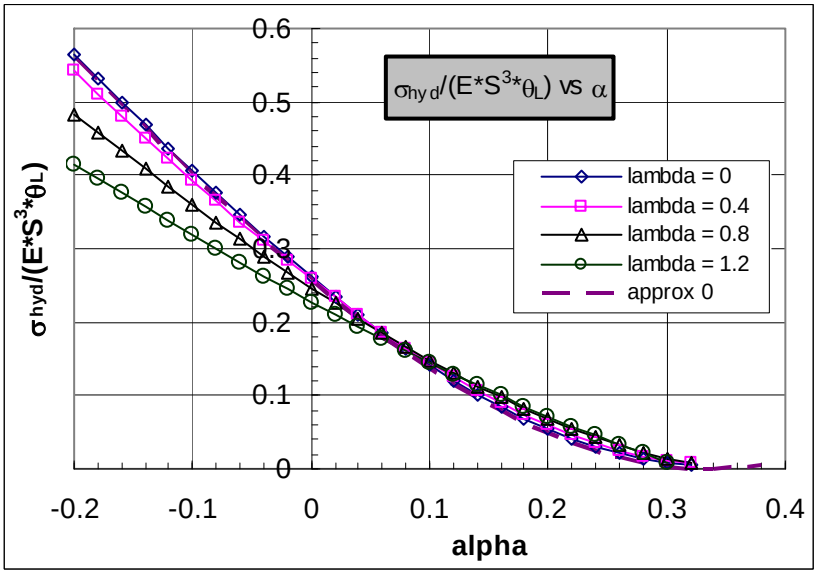

Figure F.14. Normalized Hydrostatic Stress as a Function of α and λ.

To illustrate the use of Equation (F-46) and Figure F.14, consider a bearing with bonded external plates and S = 12. It is subjected to a loading that causes ε_a = -0.01 in /in and θ_L = 0.01 radians per layer. Then

$$\alpha = -\frac{\varepsilon_a}{S\theta_L} = -\frac{-0.01}{12*0.01} = 0.0833$$

$$f(\alpha) = \frac{4}{3}\left\{-\alpha\left(1-\alpha^2\right)+\left(\alpha^2+\frac{1}{3}\right)^{1.5}\right\} = 0.154$$

$$\sigma_{hyd,\max} = ES^3\theta_L f(\alpha) = E\left(12^3*0.01*0.154\right) = 2.66E$$

Gent and Lindley (1959b) analyzed rupture under hydrostatic tension using fracture mechanics and, to confirm their findings, they conducted experiments in which they applied pure tension to small circular rubber layers bonded to external plates. They found that sudden rupture occurs when the hydrostatic tension stress reaches a stress of

$$\sigma_{rupture} \approx 0.9E \qquad \text{(F-47)}$$

The internal rupture is a consequence of the local stress state in the rubber and not the overall loading. Thus, the fact that Gent and Lindley's work was based on pure tension, but the problem here is caused by combined compression and rotation, is immaterial and use of Equation (F-47) as a rupture criterion is valid.

F.1.2 Lift-off Permitted

If lift-off is free to occur because no external plates exist, the problem becomes geometrically nonlinear, and therefore more difficult, even if the material nonlinearity is ignored on the basis that the displacements are small. An approximate analytical approach can be developed for the 2-D problem of an infinite strip, and is presented here.

Consider an infinite strip bearing layer of length L. A rigid sole plate rests on it, inclined at an angle θ, and supports a load per unit width, p, small enough that the plate makes only partial contact with the elastomer layer, as shown in Figure F.15.

The following assumption is made:

- The bearing may be divided into two parts: the one on the unloaded side experiences no vertical load and no internal stress or strain, while the one on the loaded side behaves as though the vertical edge at the neutral axis were a free surface.

The approximations implied by these assumptions are:

- The vertical (axial) stress on the unloaded region is zero. This is not quite true because the steel plate will be bent at the "neutral axis" and the out-of-plane shear stresses in it will cause some vertical stress on the elastomer.

- No interaction exists between the two regions of the bearing. This is also not quite true because the profile of the left edge of the loaded part (as shown) will not be completely free from shear strain.

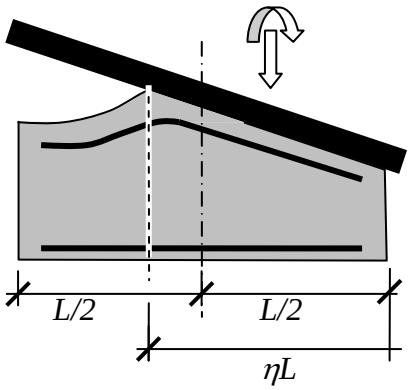

Figure F.15. Lift-off: Assumed Bearing Behavior.

The cross-section of one layer of the bearing is shown in Figure F.15. The instantaneous shape factor, S_i, of the right hand, compressed, region is given by

$$S_i = \frac{\eta L}{2t} \tag{F-48}$$

where the distance ηL is the length of the compressed region. The dividing line between the two parts of the bearing is taken to be the point at which contact is lost. The length, ηL, of the compressed region is related to the axial strain and rotation by the fact that α, as defined in Equation (F-44), has the value 1/3 for the right hand region. (This is a consequence of its being at incipient lift-off). The axial strain in the middle of the instantaneous compressed region, ε_{ai}, and the rotation angle are then related by

$$S_i = \frac{-3\varepsilon_{ai}}{\theta_L} \tag{F-49}$$

where ε_{ai} is negative if the strain is compressive, as it is expected to be. The subscript "*i*" indicates the instantaneous value, corresponding to the compressed region's covering only part of the total area of the bearing. The load per unit width on the bearing is p, (negative if compressive) and it is related to the average strain in the compressed region by

$$\frac{p}{\eta L} = \sigma_{ai} = \varepsilon_{ai} E\left(A_a + B_a S_i^2\right) \approx \varepsilon_{ai} E B_a S_i^2 \tag{F-50}$$

This can be combined with Equations (F-48) and (F-49) to give

$$S_i = \sqrt[4]{\frac{-3p}{B_a 2tE\theta_L}} \tag{F-51}$$

Equation (F-51) relates ηL, the length of the compressed region, to the loading parameters p and θ_L. (It does so indirectly, since S_i is a function of ηL). The rotation per layer, θ_L, is expressed as a multiple, ρ, of the characteristic rotation for the full bearing section, θ_c,

$$\theta_L = \rho\theta_c \tag{F-52}$$

$$\theta_c = \frac{-\varepsilon_{a0}}{S_0} = \frac{-p}{S_0^4 EB_a 2t} \tag{F-53}$$

Note that the coefficient ρ is the inverse of α, used in Section F.1.1.4. In Equations (F-52) and (F-53), the subscript 0 refers to the properties of the complete bearing, rather than the instantaneous loaded portion. The physical meaning of θ_c is that, when it is applied at the same time as the load p, the vertical displacement on the tension edge of the bearing is zero. As explained in SectionF.1.1.4, this is not the same as the initiation of lift-off. These two equations can be substituted into Equation (F-44) to give

$$\eta = \frac{S_i}{S_0} = \sqrt[4]{\frac{3}{\rho}} \tag{F-54}$$

Coefficient η defines the proportion of the bearing area that is subjected to compressive stress, and ρ defines the amplitude of the rotation. For $\rho > 3$, $\eta < 1$, lift-off occurs and the compressed region is smaller than the bearing surface.

The components of shear strain may now be computed as

$$\gamma_a = -C_a S_i \varepsilon_{ai} = C_a \frac{-p}{2tEB_a S_i^2} = C_a \frac{-p}{2tEB_a S_0^2}\sqrt{\frac{\rho}{3}} \tag{F-55}$$

$$\gamma_r = C_r S_i^2 \theta_L = C_r \frac{-p}{2tEB_a S_0^2}\sqrt{3\rho} \tag{F-56}$$

These can be added to give

$$\gamma_{tot} = \frac{-p}{2tEB_a S_0^2}\left(C_a + 3C_r\right)\sqrt{\frac{\rho}{3}} \tag{F-57}$$

Equation (F-57) may also be expressed in terms of the average stress, σ_{a0}, referred to the entire bearing surface. The stress is not real, because the load is applied only to part of the bearing surface, but it is still a convenient measure of the load. The load p causes an average stress on the whole bearing of

$$\sigma_a = \frac{p}{L} = c_\sigma G S_0 \qquad \text{(F-58)}$$

where c_σ is a dimensionless coefficient whose value may be expected to lie in the range $0.0 < c_\sigma < 3.0$. Then, using $E \approx 3G$, and ignoring the negative sign,

$$\gamma_{tot} = \frac{c_\sigma G S_0 L}{2tEB_a S_0^2}\left(C_a + 3C_r\right)\sqrt{\frac{\rho}{3}} = \frac{c_\sigma}{3B_a}\left(C_a + 3C_r\right)\sqrt{\frac{\rho}{3}} \qquad \text{(F-59)}$$

For an infinite strip and incompressible conditions, $C_a = 6$ and $C_r = 2$, so this becomes

$$\gamma_{tot} = \frac{3c_\sigma}{B_a}\sqrt{\frac{\rho}{3}} \qquad \text{(F-60)}$$

Prior to lift-off, the total shear strain may be calculated by conventional means, because the complication of the varying contact area does not exist. It can be shown that, under those conditions, the total shear strain is

$$\gamma_{tot} = \frac{c_\sigma}{3B_a}\left(C_a + \rho C_r\right) \qquad \text{(F-61)}$$

Equation (F-61) is linear in θ_L (or ρ), as might be expected, while Equation (F-59) is non-linear. At incipient lift-off, when $\theta_L = 3\theta_c$, and $\rho = 3.0$, they give the same value, as they should. The individual curves that relate γ_{tot} to ρ are valid before and after lift-off respectively, and both the curves represented by the two equations and their slopes are continuous where they meet, at $\rho = 3$.

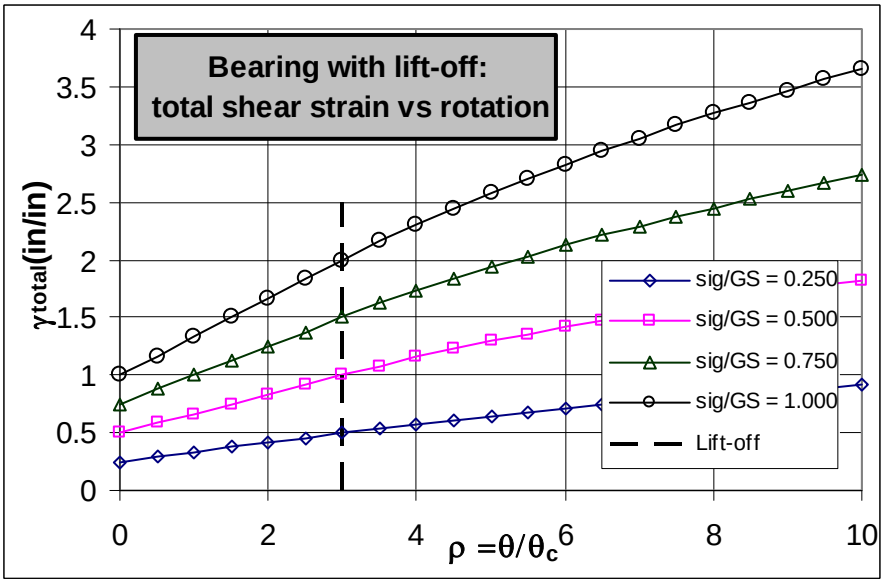

Figure F.16 shows the relationship between total shear strain and rotation angle, for a fixed load per unit width, p. Several curves, each representing a different value of p, are

shown. They are made dimensionless by expressing the loading, p, as σ_{a0}/GS_0, so that bearings of different sizes and materials may be represented on the same plot. The total shear strain is the sum of the shear strains due to compression and rotation, and is shown for the "compression" edge of the bearing layer. Each curve is a composite of Equations (F-59) and (F-61). They meet at $\rho = 3.0$, which represents incipient lift-off for all cases.

As can be seen, the curves flatten out slightly after lift-off. This suggests that the total shear strain may be approximated conservatively by using the simple expedient of ignoring the fact that lift-off occurs, and computing the components of shear strain using the linear, pre-lift-off equations (e.g. Equation (F-61)). The ratio of the "correct" shear strain, computed using Equation (F-59) and the approximate one, obtained using Equation (F-61), is shown in Figure F.17. It shows that the ratio lies in the range 0.80 to 1.0 for ρ values up to 10, and is therefore conservative. This finding was confirmed using Finite Element Analysis.

A physical explanation can be given for this finding. Consider a bearing in which lift-off has occurred. Now freeze the position of the sole plate, and pull the separated elastomer upwards so that it is once again attached to the sole plate. The elastomer in that region will experience vertical tension stress. Now release the vertical displacement of the sole plate but keep the same rotation. The sole plate will move downwards in order to re-establish equilibrium, because of the new tension stress in part of the elastomer. The bulge on the compression side will increase and the shear strains there will be larger when the elastomer is everywhere attached to the external plates. The converse is therefore true; lift-off will reduce the bulging and the shear strain on the compression side, if the rotation remains the same.

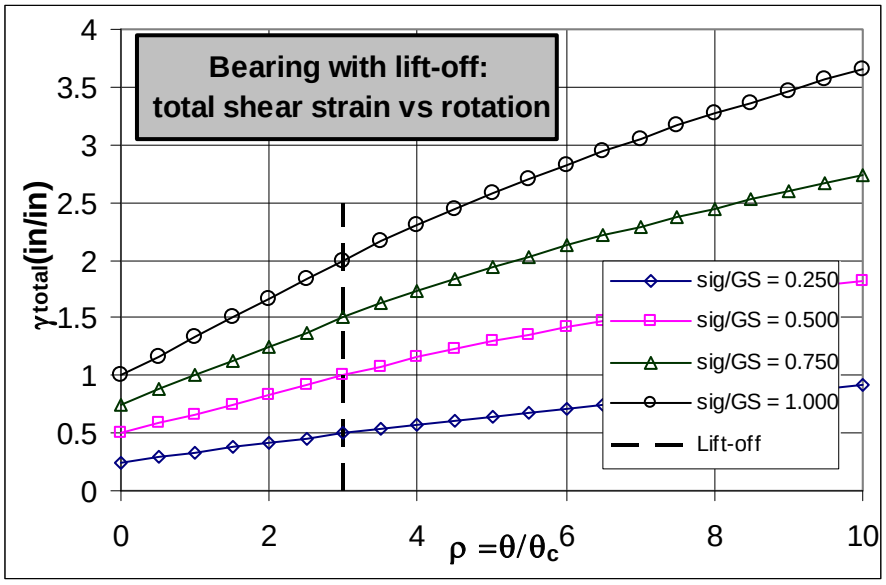

Figure F.16. Total Shear Strain for Bearing with Lift-off.

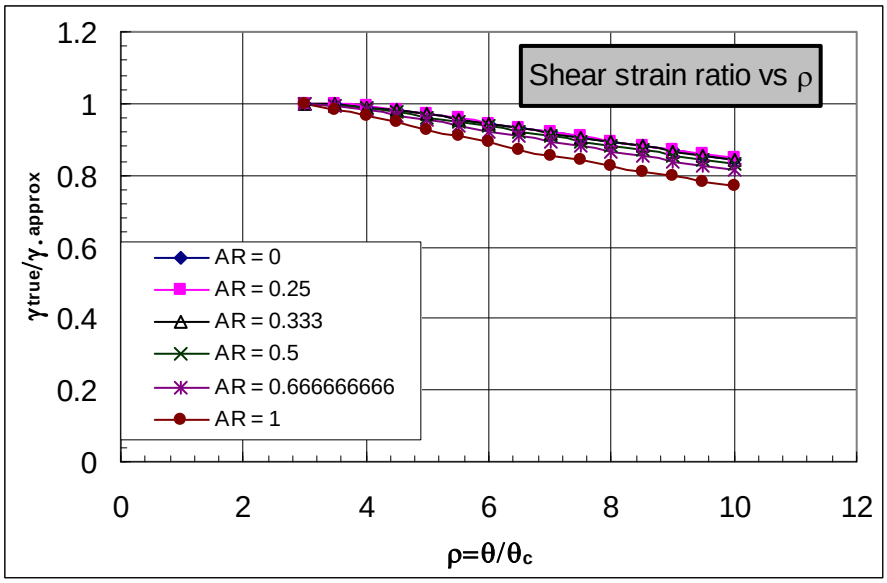

Figure F.17. Post Lift-off Conditions: Ratio of Approximate and True Total Shear Strain.

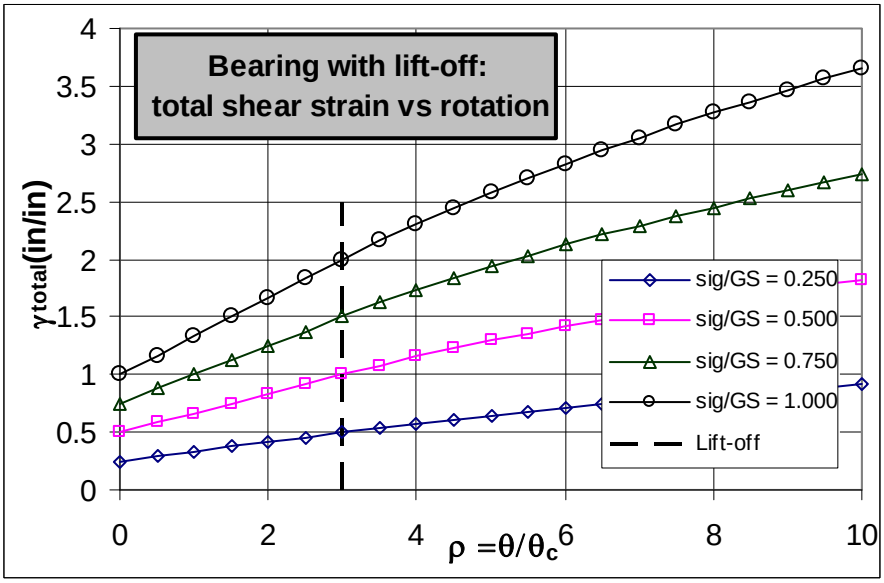

Figure F.16 leads to two observations. First, lift-off is unlikely to occur under service conditions if the bearing support and the underside of the girder are parallel under full dead load because the service rotations are likely to be too small. In that case the post-lift-off calculations are not needed. As an example, consider a bearing with S = 6, three layers, loaded to an average stress of 1.0 *GS* (approx 600 psi). Lift-off starts when

$$\theta > 3\theta_c = 3\frac{c_\sigma}{3S_0^2 B_a} = \frac{1.0}{6^2 * 1.333} = 0.0208\ rad\ /\ layer \qquad \text{(F-62)}$$

or 0.0625 radians total in the three layers. This rotation is most unlikely to be reached during the service life of the bridge. During construction, the axial load is lighter, thereby

reducing the lift-off rotation, θ_c, and the rotation is larger, in which case lift-off is possible.

Second, even if lift-off does occur, use of the "no-lift-off" equation (Equation (F-61)) causes only a small error in the predicted total shear strain on the compression side, and that error is conservative.

This discussion suggests that the linear equations (Equation (F-61) may safely be used to predict total shear strains even after lift-off. This finding simplifies design by allowing one set of equations to be used for computing shear strains under all circumstances.

F.2 Shear Strain Capacity

Two models were developed to determine shear strain capacity and to form the basis for design. One, referred to here as the Linear Model, uses Gent's linear theory to relate loads to nominal shear strains. For design, it limits to a fixed number the total nominal shear strain due axial load, rotation and shear displacements. In this model, the nominal strains due to cyclic effects are multiplied by a constant numerical factor to reflect their greater potential to inflict debonding damage on the bearing. That model is described in Section F.2.1

The second model, called the "Nonlinear Model", represents an attempt to obtain a closer fit with the data than is possible with the Linear Model. It differs in three major respects from the Linear Model. First, it uses a nonlinear relationship between the load and nominal strains. Second, the components of strain that are caused by cyclic loads are multiplied by a coefficient that is a function of the number of cycles, rather than a constant. Third, the strain capacity is not a fixed number, but is a function of the amount of debonding deemed acceptable. The nonlinear model is more complex than the linear one. It is described in Section F.2.2

Both models are described here. The Nonlinear Model was developed first. However, for reasons discussed in Section F.4, it is considered less desirable as a design procedure at this time, and the design procedure defined in Appendix G, and based on the Linear Model, is recommended for adoption by AASHTO. The Nonlinear Model is described here so that, when the necessary data become available, it may be developed into a complete and fully calibrated design procedure.

F.2.1 Linear Model

In the Linear Model, the nominal shear strains are obtained from the loads by using Gent's equations (Equations (F-24) and (F-25). The total shear strain that represents the demand on the bearing is obtained by

$$\left(\gamma_{a,st} + \gamma_{r,st} + \gamma_{s,st}\right) + c_N\left(\gamma_{a,cy} + \gamma_{r,cy} + \gamma_{s,cy}\right) \le \gamma_{cap} \qquad \text{(F-63)}$$

In Equation (F-63), the subscripts *a*, *r* and *s* refer to axial, rotation and shear responses, and *st* and *cy* refer to static and cyclic load respectively. The left hand side of the equation defines the total shear strain demand. It is expressed as a static component plus a cyclic component that is multiplied by an amplification coefficient, c_N, to account for the damaging effects of cyclic loading. The right hand side represents the shear strain

capacity, γ_{cap}, and is taken to be a constant. A similar approach has been adopted by others (e.g. BS 5400, EN1337).

Numerical values are needed for the constants c_N and γ_{cap}. They were obtained from the cyclic test data. For a particular level of debonding, the total nominal strain from each test was plotted against the number of cycles needed to reach that debonding level. An example is shown in Figure F.18. The vertical axis, labeled "Effective Strain", consists of the left hand side of Equation (F-56), in which the cyclic strains have been multiplied by a constant factor. The value used in Figure F.18 is 2.0.

To determine the best value of c_N, different values were tried and the correlation coefficient (R^2) of the data was found and plotted against the cyclic factor, c_N. The results are shown in Figure F.19, for both 25% and 50% debonding. These values of debonding, rather than the initiation of debonding, were used because of the scatter in the latter.

Even these data show considerable scatter, as demonstrated by the rather low R^2 values. However, at both levels of debonding, there is a clear trend that indicates that the largest correlation coefficient, and therefore the best fit, occurs with $c_N \approx 2.0$. That value was therefore selected. The effective strain vs. number of cycles for 50% debonding, using $c_N = 2.0$, is shown in Figure F.20.

A value for γ_{cap}, the strain capacity, is also needed. It is argued in Section F.3.1 that up to 50 million cycles of rotation, due to fully laden trucks, may be imposed on a bearing during the lifetime of the bridge. The best fit line in Figure F.18 crosses the 50 million cycle point at an effective strain of 4.7. The corresponding value for 50% debonding, shown in Figure F.20, is 5.6. The value adopted here was 5.0. The reason for doing so is that some of the tests (such as SHF5-C2, with a shape factor of 9) never reached 25% debonding, and so are not included in Figure F.18. There is no simple way to include them in the data analysis, but their effect would certainly be to raise the best fit line and to increase the strain corresponding to 50 million cycles above 4.7. If the best fit line is taken as is, the effective strain of 5.0 corresponds to 17 million cycles.

In both plots, the exact slope of the best fit line is dominated by the high-cycle data of tests CYC12 and CYC15 ($\log(N) \approx 5.5$ and 6.5 respectively). Also R^2 is not sensitive to the slope of the line, so predictions to 50 million cycles involve some uncertainty.

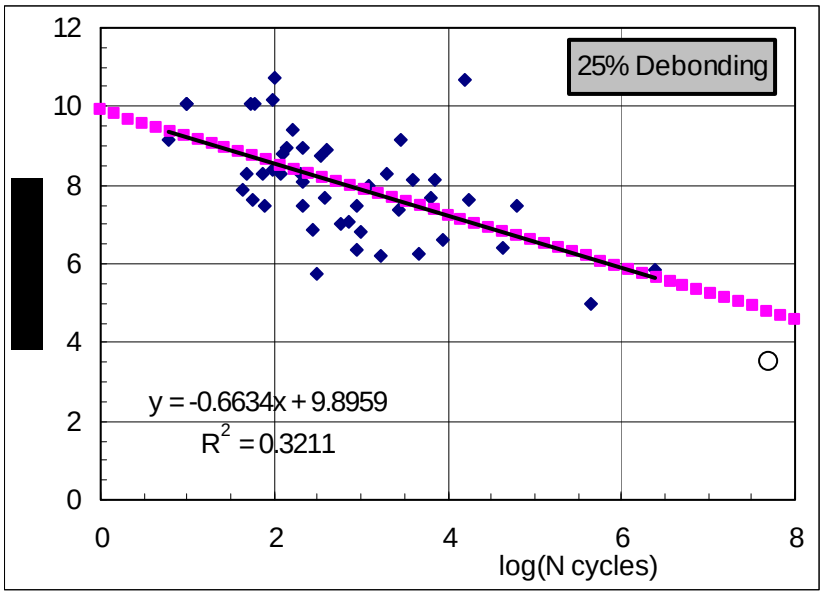

Figure F.18. Effective Strain vs Number of Cycles: 25% Debonding.

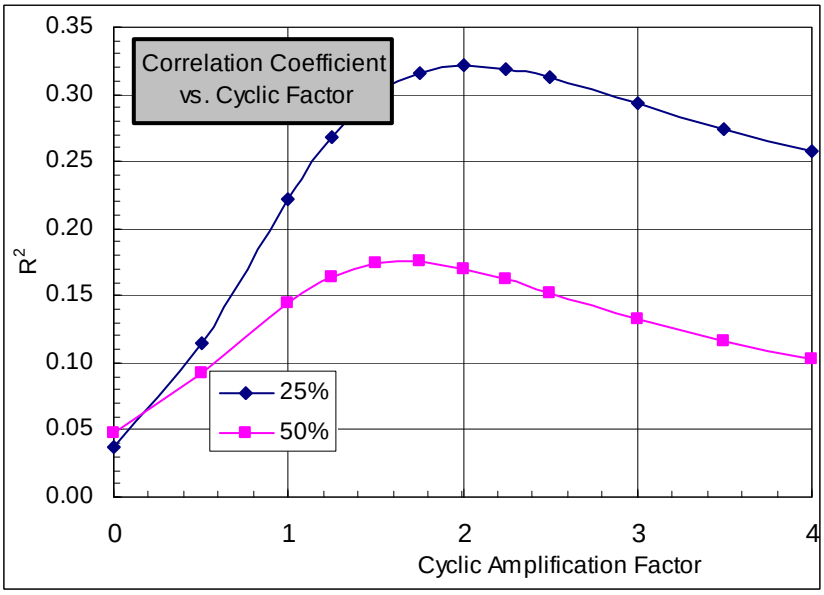

Figure F.19. Correlation Coefficient vs Cyclic Factor.

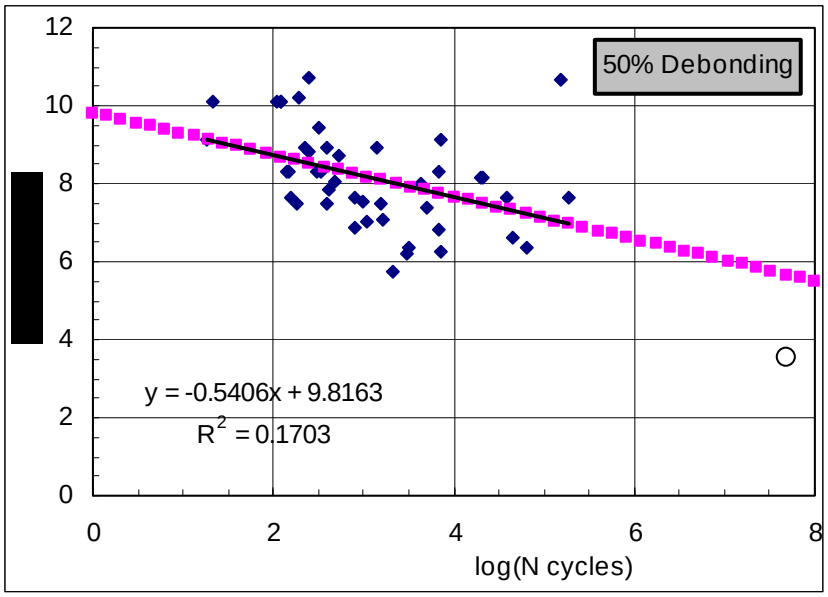

Figure F.20. Effective Strain vs Number of Cycles: 50% Debonding.

F.2.2 Nonlinear Model

F.2.2.1 Theoretical Basis.

The shear strain capacity of bearings subjected to monotonic and cyclic loading was investigated using experiments described in Appendices A, C and D. However, physical limitations prevent shear strain from being measured during the experiments. The primary difficulty is the existence of the rubber cover, but, even in the absence of cover, access to the critical location is anyway difficult because of the loading plates that enclose the bearing in the test rig. Accurate measurements were made with a micrometer depth gage of the height of the bulge in the rubber, with the intention of using them as proxies for the shear deformation. However, they proved difficult to correlate with the shear strain. Furthermore, the Finite Element studies showed that the cover provided a significant smoothing effect over the bulging of the internal layers, and that the correlation between the two was weak. Physical measurements of bulging therefore provided little useful numerical verification of the amplitude of the shear strain.

It is thus necessary to use theoretical measures to relate shear strain to load. This is done in two steps. The first is to relate the compressive load to the global, or average, compressive displacement, and this process requires consideration of bearing stiffness. The step is necessary for axial force, for which the loading is applied as a force, but is in general unnecessary for rotation, because the loading is applied as a displacement (rotation). This is so because the girder is typically so much stiffer in bending than the bearing that the rotation of both can simply be taken as the free rotation of the girder.

The second step is to relate the local shear strain in the elastomer at the edge of the shims to the global deformation measures of compressive displacement and rotation angle. The Finite Element studies demonstrated that, for small strains, the values for shear strain in

the internal layers computed by Stanton and Lund, based on Gent's theory, are valid. (The strains in some of the experiments were clearly not small, but those in field bearings are expected to be small enough that the use of the linear, small-deflection theory provides a sufficiently accurate prediction of response). However, in the edge cover, local distortions of the Finite Element mesh occur and they are sufficiently severe that the use there of the common small displacement definition of shear strain is questionable. There is also no simple way to compute the shear strains in the cover using closed-form analysis. Therefore it was decided to use the shear strain at the edge of the shim, computed in accordance with Gent's theory, as the measure of local demand on the bearing. Such shear strains are referred to here as nominal shear strains.

Obtaining the measured compressive displacement of a bearing from a known load poses some particular problems. The first is that the load-displacement curves measured in the experiments were clearly not linear, even though Gent's small-displacement theory uses a linear approximation. If the curve were linear, it could simply be projected backwards to zero load, and that point could be take as the zero for displacement. With a nonlinear curve, that is not possible. The second is that the behavior is not truly elastic. In the experiments, the first cycle typically showed response to load that was very different to that of subsequent cycles. This characteristic is usually attributed to the reversal of crystallization in the material due to the work done on it by the loading. The third is the existence of visco-elastic behavior, manifested here as hysteresis in the cyclic load-deflection curves.

An effort was made to develop a simple method for calculating compressive displacement from load, so that it in turn could be used for computing shear strains. It was based on the values recorded in the experiments. The breakdown of crystallization was addressed by using the third cycle of loading, by which time the differences with previous load cycles were negligible. The hysteresis was addressed by always using the loading, rather than the unloading, curve. (The unloading curves were always stiffer at high loads, and less stiff at low loads, as is necessary to create a hysteresis loop with positive energy dissipation). The nonlinearity was taken into account by developing nonlinear equations to define the load-deflection, or average stress vs. average strain, curves. In order to maintain consistency with small-displacement theory, the equations were chosen so that the stiffness agreed with Gent's theory at zero load. The nonlinearity was obtained empirically from the test results using Manufacturer C tests, because they included both a range of shape factors and two different aspect ratios.

Several approaches for the nonlinearity were tried. The approach that was finally selected was to use an equation for average stress of the form

$$\sigma_a = E_1 \varepsilon_a + E_m \varepsilon_a^m \qquad \text{(F-64)}$$

The first, linear, term was taken as Gent's small-displacement stiffness, and the second term was obtained by curve fitting. The curve-fits were carried out to a maximum stress of about 10 ksi, so they easily encompass all stresses likely to be used in practice. In all cases, the third cycle of the measured load-deflection curve started at about 0.5 ksi compression, because, when the tests were conducted, the primary focus was on causing

debonding damage rather than creating an accurate stress-strain curve, and some load was always maintained during the cycling to avoid temporary lift-off.

A problem was experienced that is common in interpreting bearing test results, namely the definition of zero strain. As the loading head of the test machine is lowered onto the bearing, contact is made gradually rather than suddenly, so the first part of the load-deflection plot is curvilinear and suggests a soft bearing. The problem is aggravated by the fact that the "true" zero shifts due to the de-crystallization and by the absence of data in this case below about 0.5 ksi stress. The solution adopted was to shift the data along the strain axis so as to obtain the best fit with Equation (F-56). Thus the strain shift was treated as a free variable in the curve fitting.

The best results were found with $m = 4$, and

$$E_m = 41{,}000 - 2250S \ ksi \tag{F-65}$$

where S is the shape factor. This equation gave results with an r.m.s. error in the predicted stress that was in all cases less than 250 psi.

In developing the equation, an anomaly was found with the Shape Factor 12 bearing. It was found necessary to reduce its E_1 value from the theoretical small-deflection value of $238E$ to $117E$ in order to obtain a reasonable fit. The reason for this apparently low stiffness is unknown. A Finite Element check showed close agreement with the small-deflection value of $238E$. The measured tangent stiffness at low load (i.e. $\sigma \approx 0.5$ ksi) was well below the theoretical value and was approximately the same as for the S = 9 bearing. All other bearings stiffened with load, (i.e. E_n was positive), as expected, yet the only ways to obtain a reasonable curve fit for the $S = 12$ bearing were to reduce E_1 below its theoretical value or to make E_m negative. Neither procedure makes sense. The behavior is believed not to be a consequence of the greater effect of the bulk modulus, K, on high shape factor bearings, because that is already accounted for in the B_a coefficient. The difference is therefore attributed to either unexpected rubber properties or to faulty instrumentation in the test.

F.2.2.2 Monotonic Loads

Appendix A contains results for all of the monotonic tests, including both axial and rotational loading. The shear strains corresponding to those loads were calculated using Equations (F-24) and (F-25), and are given in Table F-1. The shear strain due to shear displacements is given by

$$\gamma_s = \frac{\Delta_s}{\sum t} \tag{F-66}$$

The tests on Batch A1 bearings were not included, because the shims in those bearings had sharp machined edges and are not representative of typical field bearings. The components of shear strain were then combined to give the total that caused the initiation of debonding. The average total shear strain is 6.7, with a coefficient of variation of 14%.

Table F-1. Computed Shear Strains at Initiation of Debonding in Monotonic Tests.

Test		Shear Strain			
		Axial (in/in)	Rot (in/in)	Shear (in/in)	Total (in/in)
PMI-1a	A2	4.652	0.000	0.000	4.652
PMI-1a	B1	6.318	0.000	0.000	6.318
PMI-1a	C1	5.378	0.000	0.000	5.378
PMI-1a	D1	6.526	0.000	0.000	6.526
PMI-1c	A2	5.831	1.980	0.000	7.811
PMI-1c	B1	5.561	1.980	0.000	7.542
PMI-4	A2	3.195	2.970	0.000	6.165
PMI-4	B1	2.757	3.960	0.000	6.717
PMI-5	A2	3.687	2.970	0.000	6.658
PMI-5	B1	3.286	3.960	0.000	7.247
PMI-5	C1	3.347	3.960	0.000	7.307
PMI-5	D1	3.584	3.960	0.000	7.545
SHR1	B1	3.286	3.960	0.500	7.747
Average					6.739
st dev					0.949
CoV					0.141

These tests provided data on the computed shear strain at the initiation of debonding. It is subject to considerable scatter, but is used here because many of the monotonic PMI tests debonded little, even at very high stresses. In tests such as PMI-1a-D1, no debonding was observed at all. However the loading was never reversed, but rather increased continuously until the shims fractured at about 12 ksi applied stress. At those high loads the rubber becomes so distorted that debonding cannot be seen. Thus, the true value of the initiation of debonding in these tests could not be determined. It is known only to have occurred at an average stress higher than about 10 ksi.

The initiation of debonding described here refers to tension debonding at the shim edge. In the bearings loaded to shim failure, the shims were afterwards found to have separated from the rubber over at least part of their surfaces, so strictly they also suffered surface shear delamination as well as edge tension debonding. However, it is not clear whether that surface delamination occurred before or after the shims fractured.

The coefficient of variation of the shear strain at debonding is 14%. This is small enough to permit reliance on the data, and to base a design method, for static loads at least, on the mean value of 6.7 in Table F-1. This value may be compared with values from specifications that use a limit on total shear strain as a design criterion. For example, the previous British Specification, BS 5400 used a total shear strain of 5.0. The same value is used in the European code EN 1337, which also notes

> "The maximum value of 5.0 for ε_{td} is an empirical value which has been found from fatigue tests on three types of elastomeric bearings to best fit the limiting criterion for a strain calculated by the methode (*sic*) given here. It should not be taken to reflect the ultimate strain of the material".

Here, ε_{td} is the EN1337 notation for total shear strain. It should be noted that EN1337 provides equations for computing the components of shear strain that are based on a linear model. The nonlinear relationship between average axial stress and strain used here leads to somewhat higher compressive stresses for the same compressive strain and corresponding shear strain. For monotonic load, the European limit of 5.0 on total shear strain appears to be conservative compared with the value of 6.7 found here.

For many years, the AASHTO Specifications have imposed an independent limit of $\gamma_s < 0.5$ on the shear strain due to applied shear deformations. Those shear deformations cause shear strain in the elastomer, but they also cause local tension because the elastomer layers adopt the shape of a parallelogram, and their edges tend to roll over and, if the bond is inadequate, they may start to separate from the adjacent shims. Thus shear strains due to shear deformation are likely to be more damaging than shear strains due to axial load or rotation, and the existing limit on γ_s should be maintained. No tests using cyclic shear loading were conducted in this program. However, cyclic shear tests conducted during previous research (Roeder et al., 1987) have demonstrated the effects of amplitude of shear loading and number of cycles. The data from that study validated the use of $\gamma_s \leq 0.5$.

F.2.2.3 Cyclic Loads

Cyclic loading was applied in tests CYC 5, 7, 9, 11 and 12 to bearings from Batches A2, B1, C1 and D1. Formulation of a cyclic strain limit for the AASHTO Specification requires that those test results be represented by a system of equations that relates debonding progression to axial load, cyclic rotation amplitude and number of cycles.

Debonding does not progress linearly, so the model must reflect that fact. Plotting results on a semi-log scale shows a progression that is nearly linear on that scale, as shown in Figure F.21 for Batch B1 bearings in tests CYC 5 through 12. This suggests a basis for the relationship.

Six different approaches for creating a design model were tried. The one eventually adopted was chosen because the basis for it was rational and a good fit with the data was achieved. It is given by

$$\left(\gamma_{a,st} + \gamma_{r,st} + \gamma_{s,st}\right) + c_N\left(\gamma_{a,cy} + \gamma_{r,cy} + \gamma_{s,cy}\right) \leq g_0 + g_1 D \qquad \text{(F-67)}$$

In Equation (F-67), the subscripts *a*, *r* and *s* refer to axial load, rotation and shear displacements, and *st* and *cy* refer to static and cyclic load respectively. The left hand side of the equation defines the total shear strain demand. It is expressed as a static component plus a cyclic component that is multiplied by an amplification coefficient, c_N, to account for the damaging effects of cyclic loading.

The approach is similar to the one used for the Linear Model in Section F.2.1, but the cyclic factor, c_N is treated here as a function of the number of cycles and the strain capacity is expressed as a function of the permissible edge tension debonding, ($0.0 < D < 1.0$). The tests conducted here did not show the existence of an endurance limit, at which a specimen could be cycled for ever with no debonding. However, in every test, the specimen was loaded for a non-zero number of cycles before debonding started.

Therefore the parameter g_0, which represents the shear strain capacity for zero debonding, is included on the right hand side. The sum (g_0 + g_1) is the shear strain capacity if 100% debonding is acceptable.

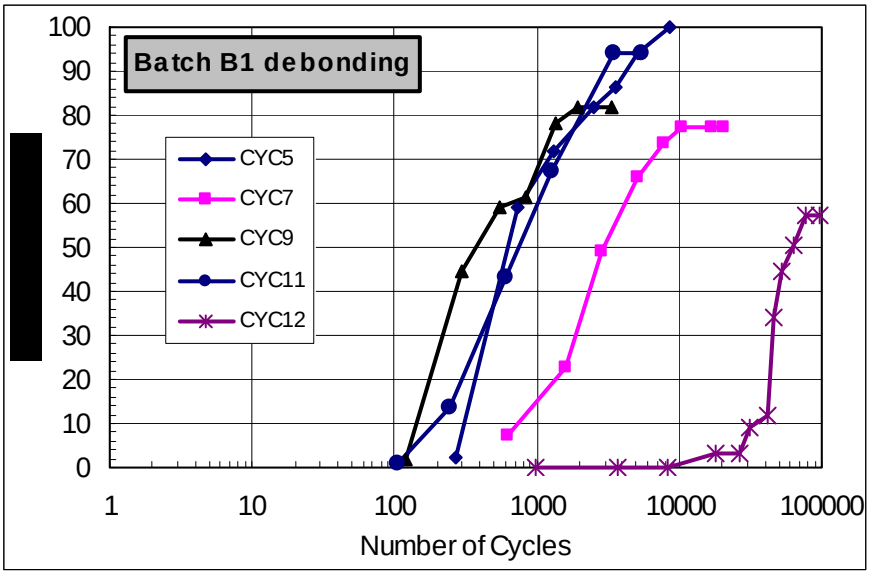

Figure F.21. Tests CYC5-12 Debonding for Batch B1 Bearings.

The challenge was to find suitable values for c_N, g_0 and g_1, with c_N being a function of the number of cycles, N. Some restrictions are needed to ensure rationality. In the interests of simplicity, g_0 and g_1, should be constants. Furthermore, c_N should be 1.0 when $N = 1$, because a single cycle may be taken to be the same as a monotonic load. c_N should also increase indefinitely with N, to reflect the absence of an endurance limit, and it should rise relatively rapidly at the start of the loading, but slow down as debonding progresses. The rate of debonding should also be a function of the intensity of the cyclic loading. (Larger rotation cycles caused faster debonding).

The simplest characterization that could be found to satisfy these restrictions is

$$c_N = 1 + \{a + b\log(N/N_{cr})\}\{1 - e^{-N/N_{cr}}\} \qquad \text{(F-68)}$$

The $\{1\text{-}e^{-N/N_{cr}}\}$ term goes from zero when $N = 0$ to 1.0 as N tends to infinity, and the variable N_{cr} controls how fast it changes. This formula reflects approximately the debonding behavior during the early cycles. N_{cr} may be thought of as a characteristic number of cycles, after which the $\{1\text{-}e^{-N/N_{cr}}\}$ term has the value (1-1/e), or 0.632.

If the $\{a + b \log(N/N_{cr})\}$ term were absent, c_N would simply vary with N from 1.0 to 2.0. However, this characterization was found not to fit the data, because, particularly in tests CYC12 and CYC15 (small rotations, high cycle numbers), the debonding damage appeared to progress without tending to a limit. Therefore the $\{a + b \log(N/N_{cr})\}$ term was added. It is a straight line on a figure such as Figure F.21, in which D, the level of debonding, is plotted against log(N), and acts as an line to which the exponential term is asymptotic.

The long-duration test, CYC15, was carried out on only one specimen (Batch C1), so Batch C1 was used for the initial fitting to the model described by Equations (F-67) and (F-68). The Batch C1 data was also the least noisy. A least–squares fit technique was first used to find the optimal parameters for each individual test. Those values varied considerably, so they were then studied to determine any functional dependence on the shear strains. It was found that b and N_{cr} correlated most strongly with the cyclic shear strain, and the best fits were found with

$$a = 1.68 \tag{F-69}$$

$$b = 2.36\gamma_{r,cy}^{-0.667} \tag{F-70}$$

$$N_{cr} = 10^{\left(3-1.8\gamma_{r,cy}\right)} \tag{F-71}$$

$$g_0 = 6.6 \tag{F-72}$$

$$g_1 = 8 \tag{F-73}$$

where

$\gamma_{r,cy}$ = cyclic component of the induced shear strain (due here to rotation alone).

The implication of Equations (F-72) and (F-73) is that the shear strain required to reach 100% debonding under monotonic load is $g_0 + g_1 = 14.6$. As pointed out above, such shear strains were never reached in the monotonic tests, because the shims failed first. Thus those tests cannot be used to confirm the value of g_1, and reliance must be placed on the cyclic test results. Doing so creates a difficulty, in that the design Equation (F-67) could be satisfied by using either a small c_N and a small (g_0, g_1) pair, or a large c_N and a large (g_0, g_1) pair. Figure F.22 through Figure F.27 show the curves of debonding vs. number of cycles for the CYC test series, sorted according to test.

The plots show that considerable scatter exists in the measured data, which fact alone makes a perfect fit impossible. In most cases, the plots have been cut off before the end of the test, so as to show more clearly the data at low debonding levels. In each case the plot shows curves from the four different test specimens and a model curve. Because the model curve (Equation (F-67)) depends on material properties (needed to obtain the compressive strain), and all the specimens had somewhat different properties, the model curve was prepared using the average G and K values. The only exception is Test CYC15, for which only Batch C1 data are available, so the model curve in that figure is based on the Batch C1 material properties. No curves are shown for Specimens A1, because they had shims with sharp machined corners, and therefore debonded at an artificially fast rate.

In general the best fit occurs with the Batch C1 data, largely because the primary fitting was done using it. (The fit between the model and the Batch C1 data was even better than that shown when the correct material properties for the C1 bearings, rather than the average for all bearings, were used in the prediction). The long-term CYC15 data was

given more weight than the others during the fitting, because it represents most closely the loading conditions to be expected in practice.

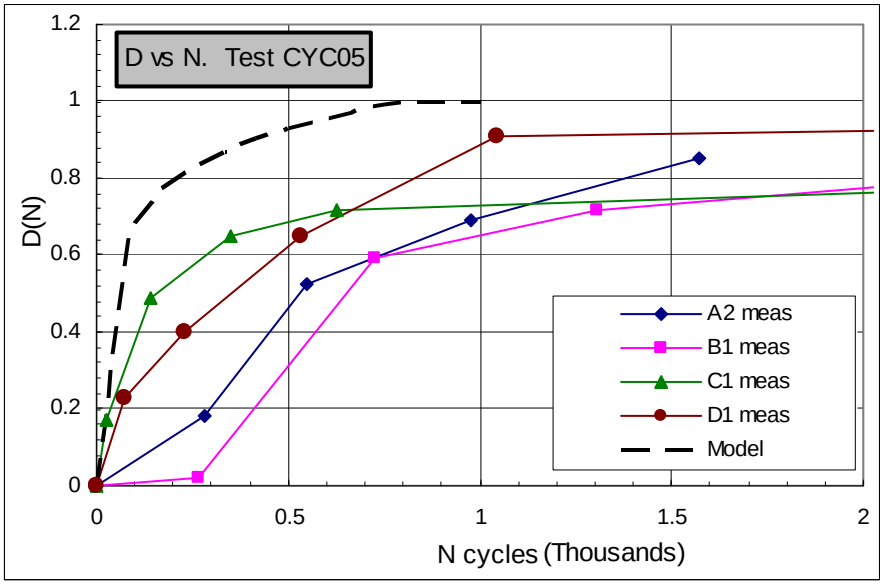

Figure F.22. Debonding vs. Number of Cycles. Test CYC05.

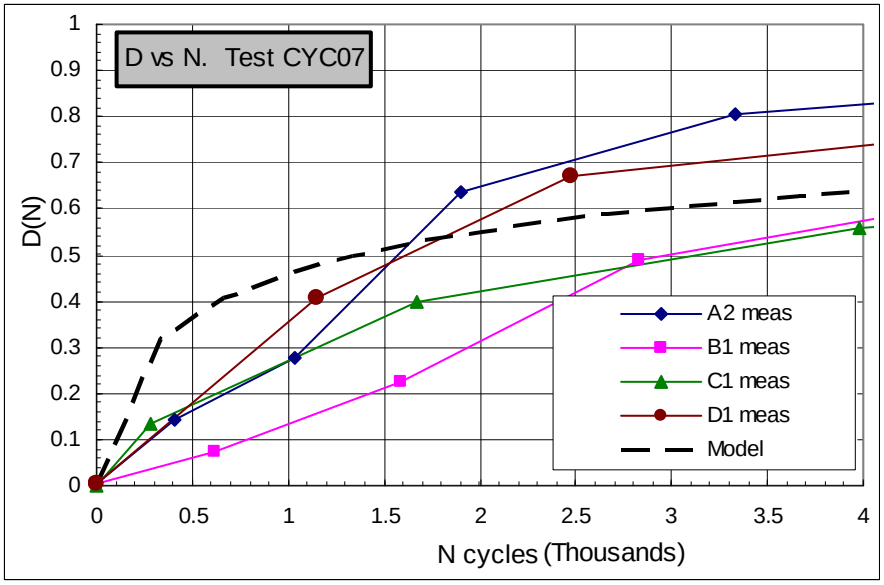

Figure F.23. Debonding vs. Number of Cycles. Test CYC07.

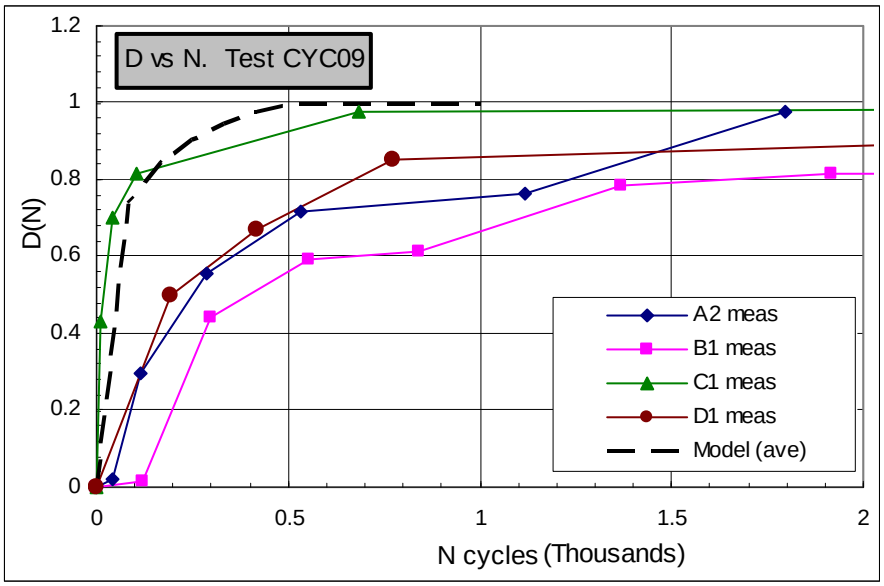

Figure F.24. Debonding vs. Number of Cycles. Test CYC09.

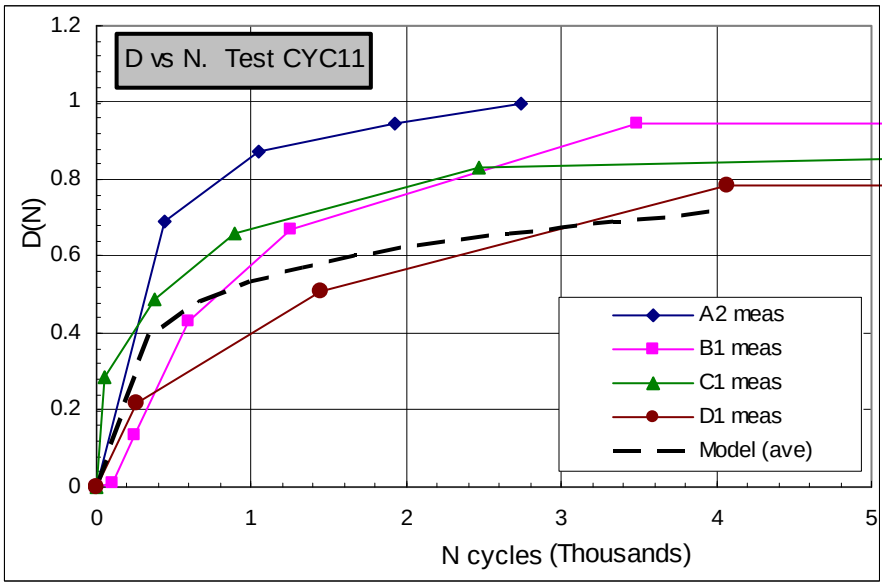

Figure F.25. Debonding vs. Number of Cycles. Test CY11.

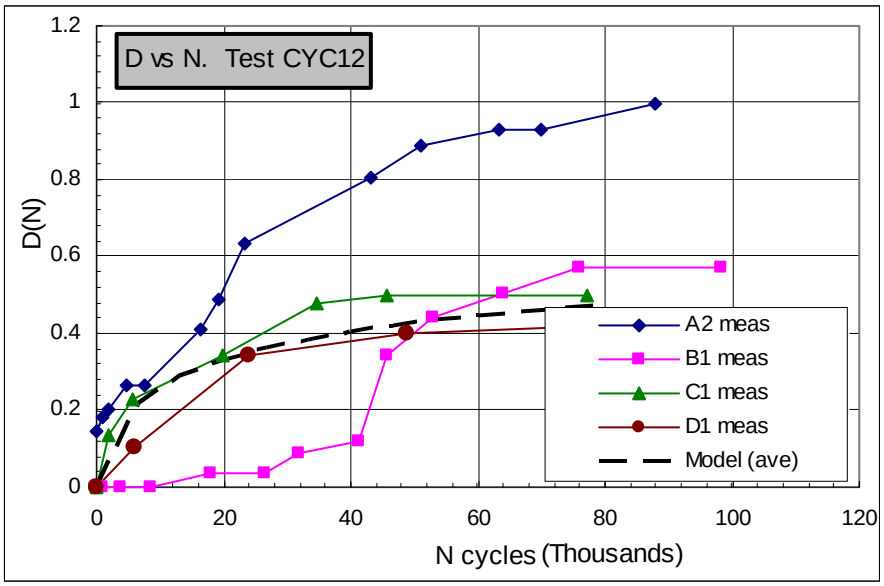

Figure F.26. Debonding vs. Number of Cycles. Test CYC12.

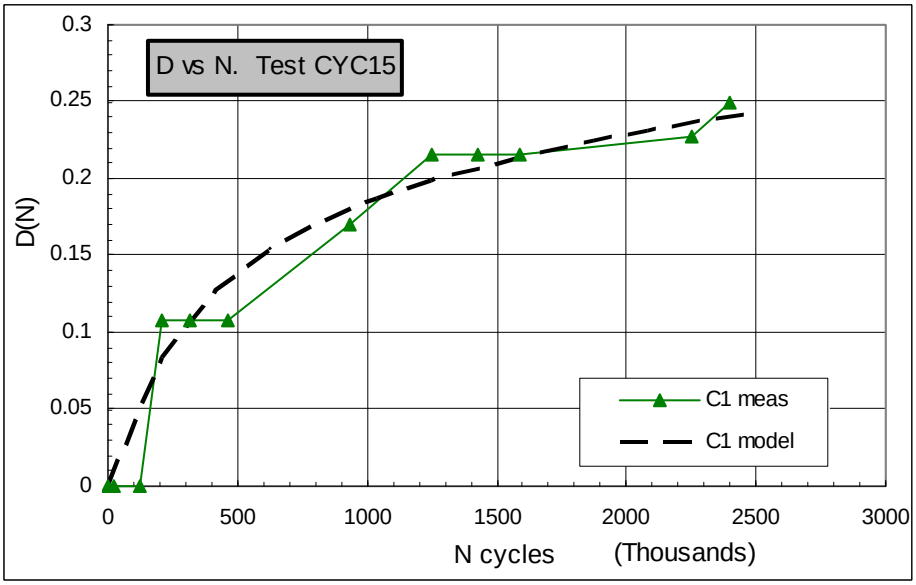

Figure F.27. Debonding vs. Number of Cycles. Test CYC15.

Equations (F-67) through (F-73) are rational, but they are quite complicated. They could be programmed into a spreadsheet or other application, in which case their complexity becomes irrelevant, but their use in the AASHTO Specifications may raise questions. Therefore, an effort was made to express the data differently, in the hopes of simplifying the Nonlinear Model.

Figure F.28 through Figure F.30 show the measured data expressed in the conventional form used for fatigue data: an S-N plot, in which the number of cycles is plotted on a log scale. The three plots show results for 25%, 50% and 75% debonding. Most of the values

were obtained by interpolating between real measurements, because the latter were taken at irregular intervals. The curves labeled "A2" etc. refer to specific bearings, "mean 1875" refers to the mean of all bearings tested at 1875 psi, and "25% opt" is the theoretical curve that best fits the 25% debonding data.

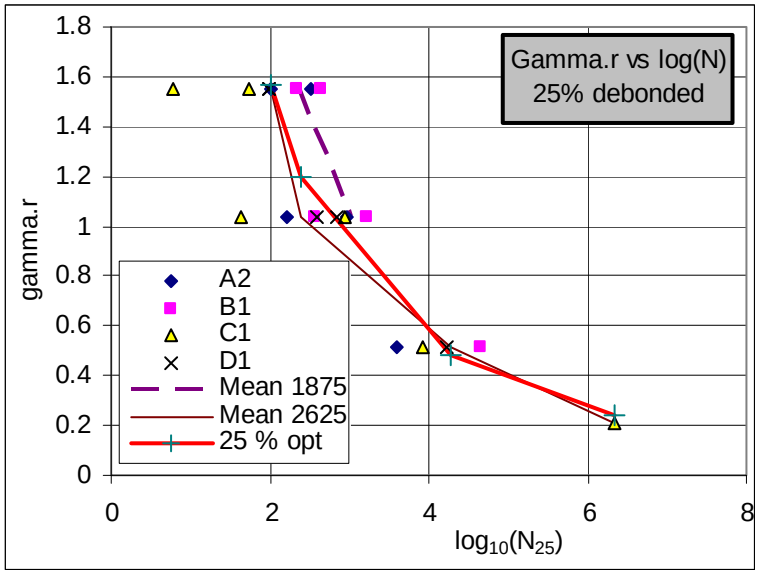

Figure F.28. Fatigue Life for Cyclic Shear Strain due to Rotation: 25 % Debonding Criterion.

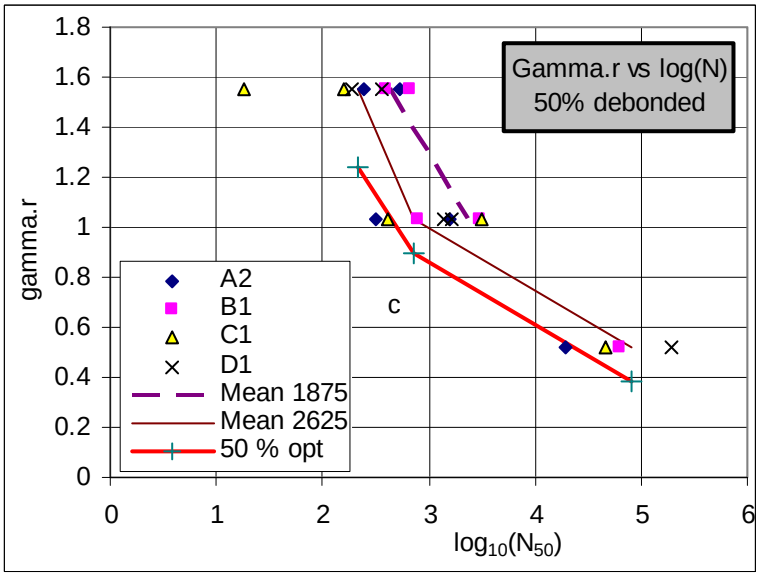

Figure F.29. Fatigue Life for Cyclic Shear Strain due to Rotation: 50 % Debonding Criterion.

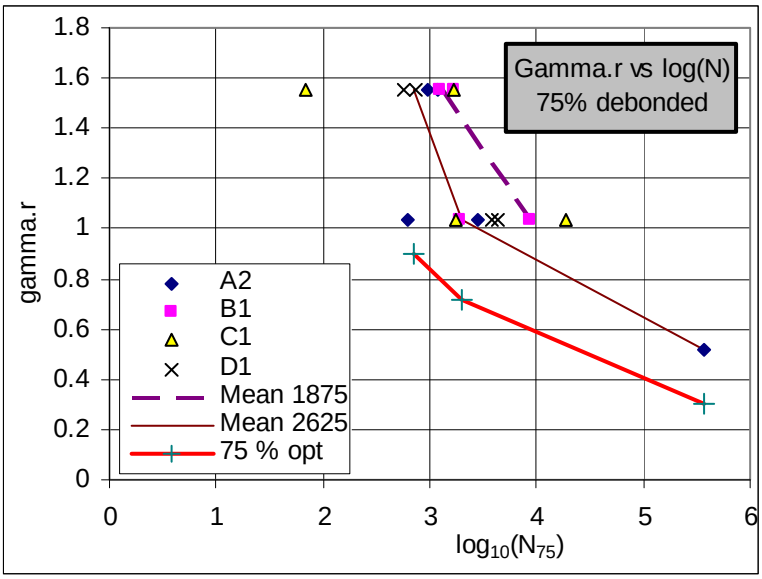

Figure F.30. Fatigue Life for Cyclic Shear Strain due to Rotation: 75 % Debonding Criterion.

Several observations can be made. First, the scatter in the data is considerable, even when using the semi-log scale, which tends to conceal differences by compressing the data along the horizontal axis. Second, a definite trend exists of increasing number of cycles with decreasing cyclic shear strain. Third, an increase in static axial shear strain decreases the fatigue life of the bearing.

Each of these three characteristics is to be expected. However, the goal is to develop a model that predicts the cyclic shear strain (here expressed as the rotational shear strain, because in the tests that was the only shear strain that was cyclic) as a function of the number of cycles, the static (axial) shear strain and the level of debonding acceptable. It is worth recalling that γ_r, the cyclic rotational shear strain the field, is likely to be on the order of 0.1 in practice, so it falls well below any of the data points, and any model will have to rely on extrapolation beyond the measured data.

The data show no sign of an endurance limit when plotted in this form, at least within the range of γ_r studied in the tests. Thus there is no basis for creating the bilinear S-N curve often used to characterize fatigue data. A second possibility would be to fit a single straight line to the data. However, that is at odds with the clearly curvilinear shape of the 25% debonding curve. Furthermore, for the 50% debonding data, the straight line would predict that, with a cyclic γ_r of zero, 50% debonding would be reached after about one million cycles. That prediction is clearly not rational.

The mean values of γ_r vs. log(N) were plotted and they suggested a gradually descending curve, so a modified hyperbola was fitted to them. It had the form

$$\gamma_r = \gamma_{r0} + \frac{a}{\left(\log(N) - N_0 + c_a \gamma_a\right)} \qquad \text{(F-74)}$$

Where γ_{r0}, a, N_0 and c_a are constants to be determined by calibration. In the absence of axial load, the cyclic rotational shear strain capacity would become infinite when log(N) reached N_0. This is not rational, but is a consequence of trying to choose a simple form for the curve.

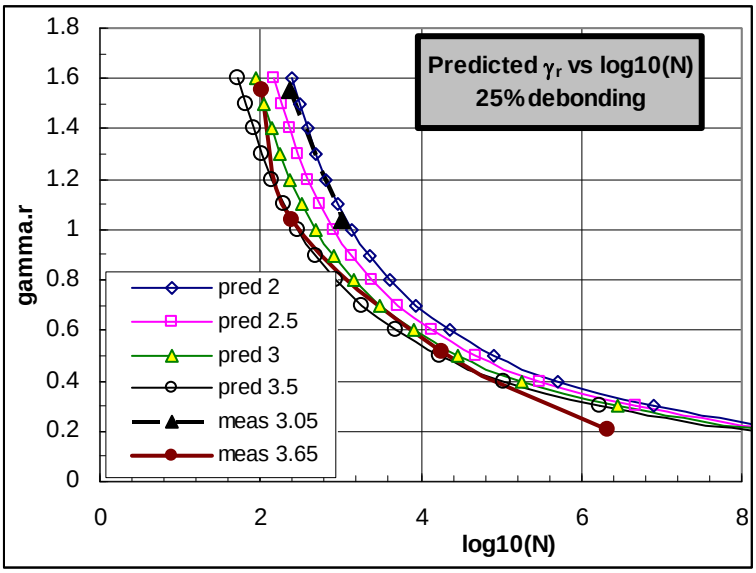

Figure F.31. Fatigue Life for 25 % Debonding Criterion. Equation (F-67) vs Measured Data.

The constants were evaluated for each of the three debonding levels shown, and functional relationships were sought between the constants and the input variables D (debonding level) and γ_a. The parameters γ_{r0}, a and c_a were found to be nearly constant. N_0 was found to depend modestly on D. The final values chosen for the best fit were γ_{r0} = -0.0925, a = 2.295, N_0 = 1.937 + 1.38D, and c_a = 0.447. Predictive curves using these values are shown in Figure F.31 for D = 0.25.

The curves are prepared for different γ_a values (from 2.0 to 3.5). They appear close together in the figure because of the semi-log presentation, but the bearing with the lowest axial load (γ_a = 2) has a fatigue life that is about 10 times as long as the one with the highest load. The mean values from the measured data at γ_a = 3.05 and 3.65 are also shown. The fit appears acceptable, but it diverges significantly at low γ_r (high N). The curves predict very long fatigue lives (e.g. > 10,000,000 cycles to reach 25% debonding) for all the axial load levels shown. However, little faith can be placed in those predictions, because they represent significant extrapolations on a semi-log plot. This difficulty is illustrated by the fact that the straight line approximation to the data predicts 25% debonding at 1 million cycle of γ_r = 0, whereas the curvilinear approximation predicts a fatigue life of 100 million cycles at γ_r = 0.2. That is a very large range of predicted life, obtained from two apparently reasonable extrapolations from the test data.

The curves thus show that this representation of the fatigue data shows patterns that might be expected, but the representation does not lead to a model that is simple but reliable. The main difficulty in implementing it is the lack of data at low strain and high numbers of cycles.

F.2.2.4 Summary on Nonlinear Model

The Nonlinear Model has been shown to have advantages and disadvantages compared with the Linear Model. Its main advantage is that it reproduces the test results in a more detailed manner. It does so by relating the damage to the number of cycles of rotation at all cycle numbers (i.e. many points per test), whereas the linear model simply addresses the conditions at the end of the test (i.e. one point per test). The primary drawback discussed here is its greater complexity. However it has other drawbacks, which are discussed in Section F.4. Those drawbacks prevent the model from being used now, but the description of the model ahs been retained so that it may be developed when the necessary cyclic axial load data become available.

F.3 Axial and Rotation Demands from Dead and Live Loads.

Design requires consideration of both demand and capacity. During the conduct of the project, much of the effort was focused on establishing bearing capacity, using a combination of physical testing and Finite Element Analysis. In this section the issue of demand is investigated, using analysis.

F.3.1 Background and Assumptions

When a truck crosses a bridge, it imposes on the bearings a combination of vertical load and rotation. The relative magnitudes of those two effects vary with the truck's location. For example, the vertical load is largest when the truck is near the support, whereas the rotation is largest when the truck is near mid-span. The precise values of the load effects also depend on bridge characteristics such as continuity and skew.

Since both loadings induce strains in the elastomer, they should be considered together in design. Ideally, every possible location of the truck should be analyzed separately, and the one that imposes the largest combined strain in the elastomer should be used. However, this procedure is likely to be too time-consuming for practical design, so a simpler approach is desirable.

The traffic loading provisions in the AASHTO LRFD Specifications consist of a series of concentrated loads from a standard truck or tandem axle plus a distributed lane load. (This is a departure from earlier versions of the Standard Specifications, in which the more severe of the two was used alone, rather than both together). During the testing conducted during this research, it was found that the bearings exhibited fatigue-like behavior, in that damage accumulated and worsened as the number of cycles increased. It is therefore necessary to estimate not only the number of cycles likely to be applied in practice, but also to define what constitutes a cycle.

For truck or tandem axle loading, this is relatively straightforward, but for the lane loading it is less obvious. If the lane loading is viewed as representing lightly loaded

large trucks, then passage of such vehicles does indeed cause discrete cycles of load, and the lane load should be treated as contributing to the cyclic loading. If the lane load is viewed as representing a stream of light traffic, such as automobiles, then, in the extreme case of a continuous stream, the stream causes a constant, rather than a cyclic, load.

Counting the full lane loading in the cyclic load would imply that a train of traffic of length *l* (the bridge span length) and of intensity 0.64 kips/ft (the specified lane load), acted on the bridge for an instant, followed by a period with no lane load at all, followed in turn by the presence of a second traffic train identical to the first, and so on. Observation of light traffic on bridges suggests that this pattern does not occur. The intensity of the 0.64 kip/ft lane load is also significantly higher than that imposed by average automobiles (about 0.20 kip/ft, even in bumper-to-bumper stationary traffic).

Use of a reduced value of the lane load for the purposes of estimating cyclic loading therefore seems appropriate. This is in accordance with the fact that it is not considered as contributing towards fatigue loading for steel bridges. The full value should still be used for estimating maximum possible static load.

The amplitude of the rotation depends strongly on the girder span, stiffness and continuity, and slightly on other details such as the lateral distribution of wheel load effects among adjacent girders. Bridge curvature and skew also lead to additional complications, such as bi-axial rotation of the bearings. Computing the exact rotation could therefore be time-consuming. However, an approximate upper bound to the rotation can be derived from the limit of *l*/800 (in AASHTO LRFD Section 2.5.2.6.2) on live load deflection at mid-span, and this may be used to obviate the need for more complex calculations.

The variables that are important in estimating demand on the bearings are:

- Bridge overall dimensions (span, girder spacing, skew, continuity).
- Bridge deck physical properties (deck weight, girder stiffness).
- Load details (truck, tandem and lane loading, axle spacing, lateral distribution of wheel loads, number of cycles, direction of traffic flow).

In the analyses that were conducted, the following assumptions were made:

Span: a range of spans was considered.

Girder spacing: a range of girder spacings, consistent with normal practice, was considered.

Skew: In the interests of simplicity, skew was ignored when estimating the magnitude of the primary rotation.

Continuity. The bridge girders were assumed to be simply supported, because this condition gives the largest rotations. A correction factor was derived that accounts approximately for continuity under live load.

Deck weight. The deck was assumed to be 11 inches thick (for purposes of estimating weight) and made from normal weight concrete. The value was derived from an assumed 8 inch thick deck, with a 3 inch deep pad over the girder flanges (assumed to occupy half

the deck width), plus a 1.5 inch allowance for a wearing surface. The results of the analyses were found to be relatively insensitive to the exact deck weight.

Girder stiffness. Both steel plate girders and precast, prestressed concrete girders were considered. For a given span, steel girders generally lead to slightly lower dead loads, but to slightly higher cyclic end rotations of the girders.

Truck and tandem axle loading. A preliminary investigation showed that the truck loading almost invariably gave the more severe effects. It was used exclusively in the main analyses. Furthermore, AASHTO requires different axle spacings to be considered, but the shortest (14 ft) was found to control in all cases and was used throughout the analyses.

Lane loading. Factors were introduced into the analyses that allowed inclusion in the cyclic effects of any desired fraction (from 0.0 to 1.0) of the rotation and compressive load due to the lane loading. Different values were tried during the analyses.

Lateral distribution of wheel loads. In the interests of simplicity, the "lever rule" was used, whereby each girder was assumed to carry (s/12) times the load in one lane, where *s* is the girder spacing in feet, and a lane is assumed to be 12 ft wide.

Number of cycles. Different numbers of load cycles were considered. The largest number was 50 million. This was derived by assuming a bridge with an ADT (average daily traffic count) of 80,000 vehicles per day, of which 5% were assumed to be fully laden trucks, and a 50 year life span. Two-thirds of the trucks were assumed to be traveling in the inside lane, which is therefore the critical one. This loading represents a heavily traveled freeway. Other bridges may experience significantly fewer cycles of full truck loading.

F.3.2 Methodology

A spreadsheet was constructed that computes girder rotations and deflections and bearing rotations and axial loads, for different inputs. It was used to investigate the effects on response of varying the input parameters.

F.3.3 Computed Values

F.3.3.1 Upper Bound to Rotation.

The upper bound to the end rotation may be obtained as follows. For a uniformly distributed load acting on a simply supported girder, the end rotation is

$$\theta = \frac{1}{24}\frac{wl^3}{EI} \qquad \text{(F-75)}$$

And the mid-span deflection divided by the span length, Δ/l, is

$$\frac{\Delta}{l} = \frac{5}{384}\frac{wl^3}{EI} \tag{F-76}$$

The ratio between the two is then

$$\theta \Big/ \frac{\Delta}{l} = \frac{1}{24} \Big/ \frac{5}{384} = 3.2 \tag{F-77}$$

Similar calculations for a single concentrated load at mid-span give a ratio of 3.0. (This calculation considers the load to be located at mid-span and ignores the fact that maximum end rotation occurs when the load is at 42%, not 50%, of the span. However, the simplification introduces an error of less than 3%). Since the truck loading consists of a series of point loads, its effects must lie between those of a single concentrated load and a uniformly distributed load. The corresponding ratio for it must therefore lie between 3.0 and 3.2. The largest girder end rotation consistent with a live load deflection of *l*/800, for any longitudinal distribution of loads, is then

$$\theta \le \frac{3.2}{800} = 0.004 \tag{F-78}$$

The end rotation for any other deflection limit can be obtained directly by scaling.

If the girders are continuous over two or three spans, the mid-span deflections and the end rotations (at the central support) are multiplied by the factors in Table F-2. Because in a multi-span bridge the end rotation decreases more than the mid-span deflection, the net effect is to reduce the end rotation if the mid-span deflection is still controlled by the *l*/800 limit. If the entire load is treated as distributed, the largest possible end rotation is (0.50/0.70)*(0.004) = 0.00286 radians for two spans, and (0.40/0.52)*(0.004) = 0.00308 radians for three spans.

Table F-2. Multipliers for Rotation Angle due to Girder Continuity.

Loading	N spans		2	3
Distributed	θ/θ_0	cont. end	0.500	0.400
	θ/θ_0	free end	0.750	NA
	Δ/Δ_0		0.700	0.520
Concentrated	θ/θ_0	continuous	0.500	0.400
at mid-span	θ/θ_0	free	0.750	NA
	Δ/Δ_0		0.719	0.550

F.3.3.2 Critical Combination of Compression and Rotation

Because the end rotation and compressive load from the live loading do not reach their individual maxima simultaneously, the critical end rotation is likely to be smaller than that predicted by the foregoing values. The critical end rotation is the one that causes the largest shear strain in the elastomer of the bearing when the compressive load acts at the

same time. The calculation does not lead to a unique value, because bearings of different sizes and shapes may be chosen, some of which may be more sensitive to rotation, and some more sensitive to compressive load.

To obtain an approximate value of the critical rotation, calculations were conducted to investigate the effects of a range of parameters, such as girder stiffness, span, etc. In each set of analyses, only a single parameter was changed. The bearings were standardized by sizing them so that the total rubber thickness was *l*/1000, the dead load compressive stress was 600 psi, the aspect ratio was 2.5 and the shape factor was 6.0. In most cases, this procedure resulted in a non-integral number of layers. While this is clearly impossible in practice, it was accepted here to ensure consistency among the analyses. The girder dimensions were not intended to represent any particular girder type or size, and had no significance other than generating a value of bending stiffness.

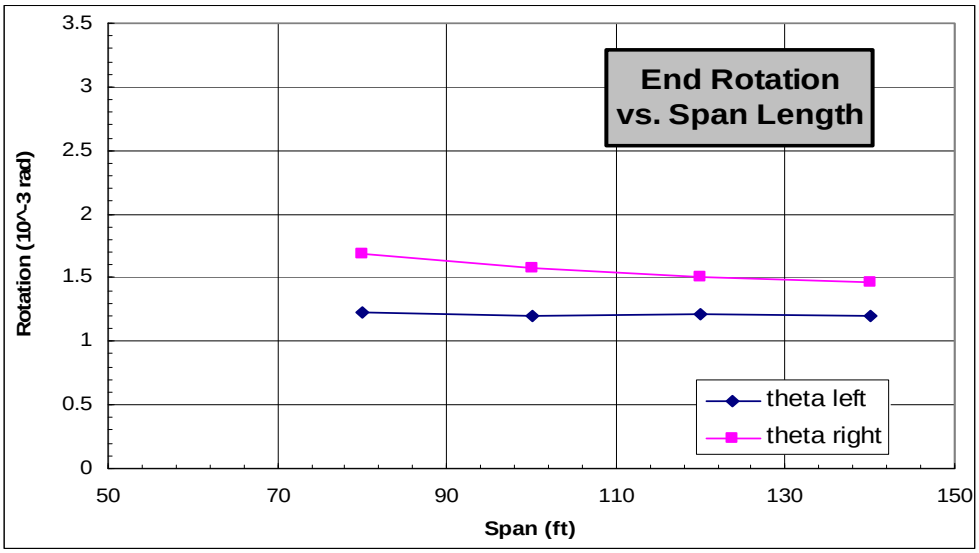

Figure F.32. Effect of Span on Rotation Angle.

The effect of span is shown in Figure F.32. The critical rotation remains nearly constant at all spans investigated, but the left and right bearings experience different rotations because the axle loads of the truck are not symmetric. (The truck traveled from left to right in the analyses). The slight reduction in rotation with increasing span length is attributed to the changes in the relative influences of the truck and lane loads. For both ends of the girder, and for all spans considered, the critical combination occurred when the extreme axle of the truck was just entering or leaving the bridge. This finding also held true for all the other parameters considered.

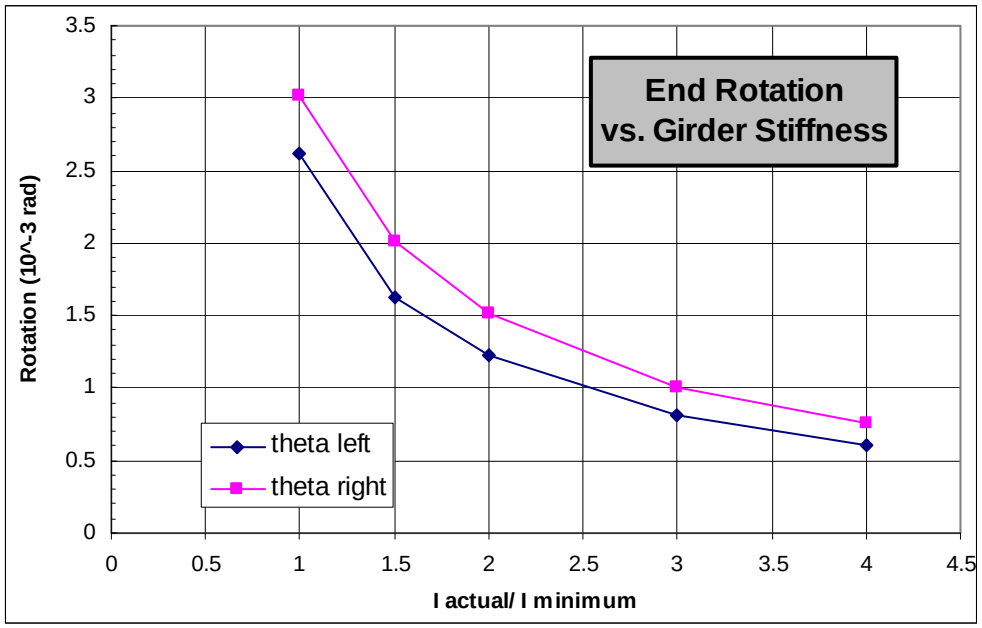

Figure F.33. Effect of Girder Stiffness on Rotation Angle.

The effect of girder inertia is shown in Figure F.33. The critical rotation is inversely proportional to $I_{actual}/ I_{minimum}$, as might be expected. ($I_{minimum}$ is the minimum girder inertia needed to ensure $\Delta < l/800$). However, even when $I_{minimum}$ is used, the rotation is still only 0.003 radians.

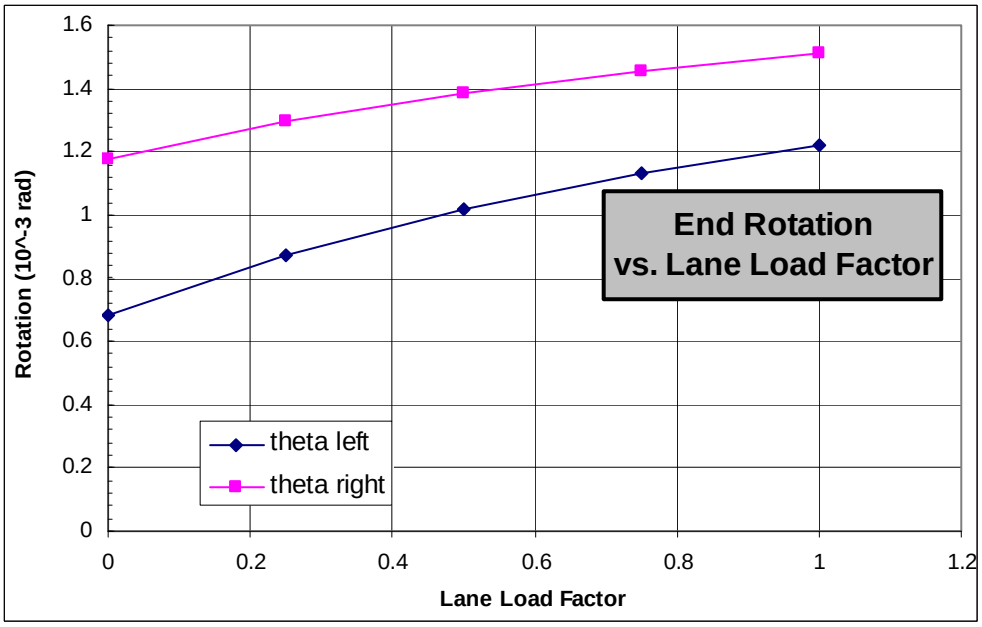

Figure F.34. Effect of Lane Load Factor on Rotation Angle.

Figure F.34 shows the effect of the lane load factor. It is relatively small and is controlled by the rotation of the bearing at the right hand end of the bridge. Reducing the

lane load to 50% of its nominal value only reduces the rotation from 0.0015 to 0.0014 radians.

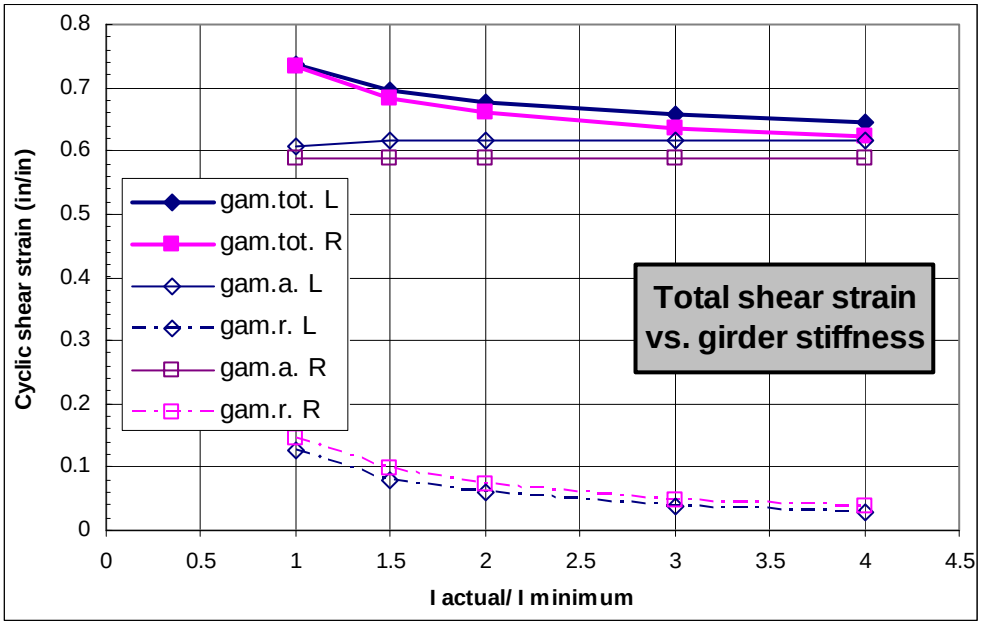

Figure F.35. Effect of Girder Stiffness on Total Shear Strain.

Girder inertia thus has the greatest effect on bearing rotation. To demonstrate its effect on the shear strains in the elastomer, cyclic shear strain in the bearing is plotted against girder inertia ratio in Figure F.35. The shear strains are those caused by the critical combination of axial load and rotation, so the total is the sum of the two individual values. The figure shows that the axial load effects provide the great majority of the total shear strain, particularly when the inertia ratio is high. It is thus important to include cyclic axial load with the cyclic rotation when evaluating the response of the bearing.

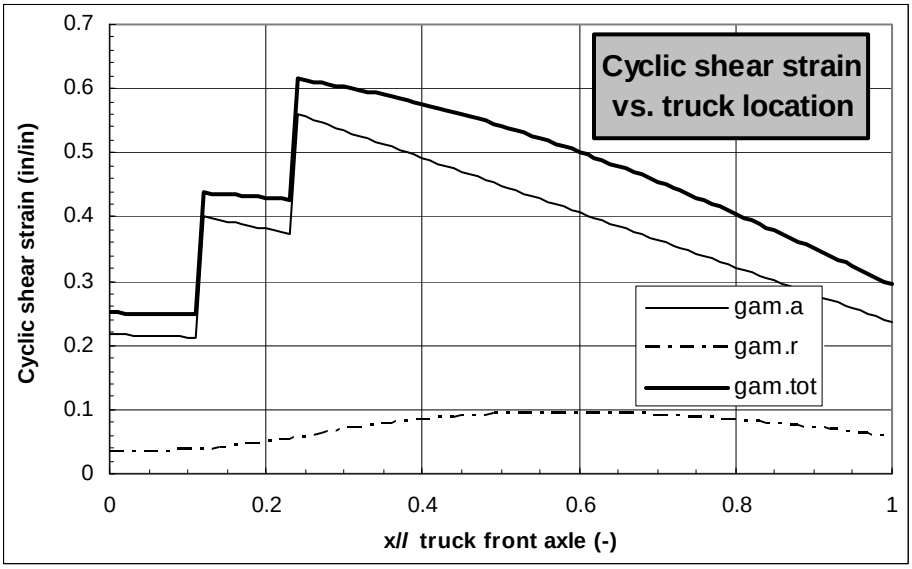

Figure F.36. Effect of Truck Location on Maximum Shear Strain.

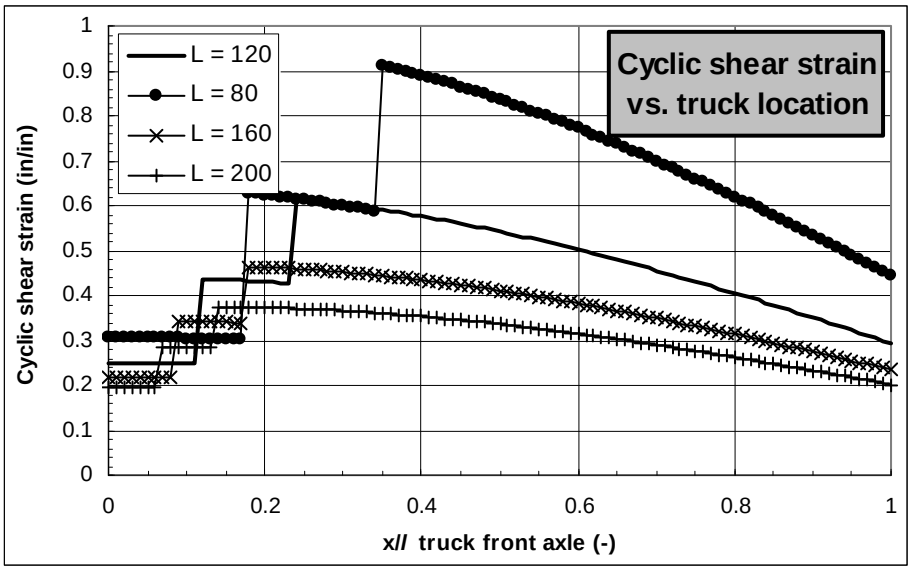

Figure F.37. Effects of Span and Truck Location on Maximum Shear Strain.

Figure F.36 and Figure F.37 further illustrate the relative importance of the axial and rotation components of the cyclic loading. Figure F.36 shows how the shear strains vary with truck location for the standard values of all parameters. The ordinate in the plot is the *x/l* value of the truck front axle as the truck travels from left to right across the bridge, and the abscissae are the shear strains in the left bearing, which experiences the largest strains. The jumps in the curve occur as the various truck axles enter the bridge. The shear strain due to rotation is non-zero when $x/l = 0$ because the full lane load is assumed to be in place. The axial load clearly dominates the cyclic loading effects.

Figure F.37 shows similar information, but for a range of span values. For clarity, only the total shear strain is shown. The cyclic shear strains due to axial load decrease as the span increases because a larger bearing is needed to accommodate the larger self-weight, but the truck weight remains unchanged. The details of the relationship depend on the fact that, for these calculations, the bearing was designed so that static dead load caused an axial stress of 600 psi, as described above, but the finding is expected to be valid in principle for any practical assumptions. Figure F.37 also shows that, at very long spans, the maximum cyclic shear strain no longer occurs when the rear axle of the truck just enters the bridge, but rather when the truck is slightly further advanced. This implies that, for the great majority of bridges, the bearing may be designed with the rear axle at the end of the bridge, and only for very long bridges (greater than 201 ft. for the assumptions used here) is there a need to investigate other truck locations. Even then, use of the true critical truck location will not greatly affect the result because the curves in Figure F.37 are relatively flat near their peaks.

F.3.4 Thermal Camber

Thermal effects can cause camber in the superstructure. It is typically largest when the sun shines on the deck, which absorbs radiant heat and expands. In this section the

magnitude of the girder end rotations, and thus the rotation imposed on the bearing, are examined.

The thermal gradient to be used for design is defined in Section 3.12.3 of the AASHTO LRFD Design Specifications, and is shown in

Figure F.38. In order to evaluate the expected end rotation, the thermal gradient was applied to a series of superstructures consisting of a slab and girder. The system consisted of a 74 in. deep precast girder with an 8in. deck and a 3 in. pad of cast in place concrete between the two. Girder spacing was 8 ft. Span was 120 ft.

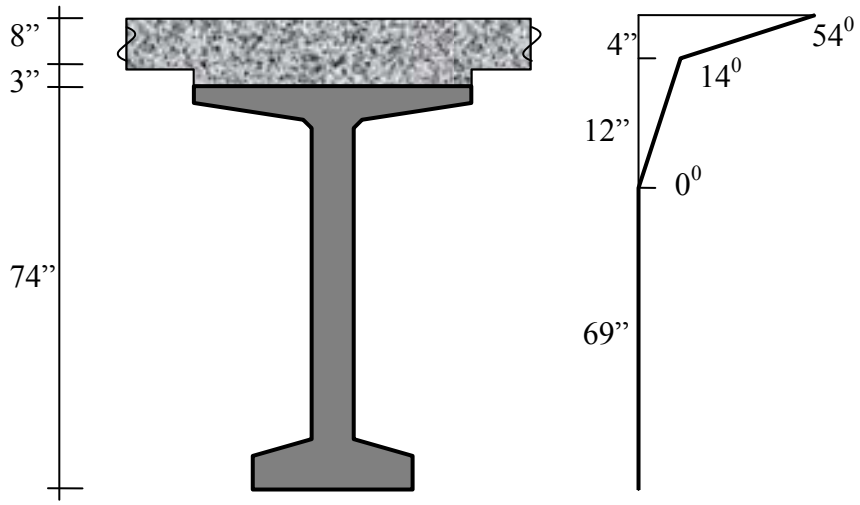

Figure F.38. Girder and AASHTO /Design Thermal Gradient (Zone 1).

The AASHTO thermal gradient caused a curvature of 1.78 x10^{-6} radians/in, which led to a mid-span upward camber of 0.461 in. and end rotation of 0.00128 radians. Thus the thermal end rotation is of the same order of magnitude as that due to truck loading. To investigate the effects of span length, a series of girders was analyzed. In the interests of simplicity, all the girders were identical except that the web height was increased. Therefore, most of them do not correspond exactly to a particular real girder. The span was also increased to achieve a constant overall span/depth ratio of 18.5, including the slab. The resulting end rotations are shown in Figure F.39.

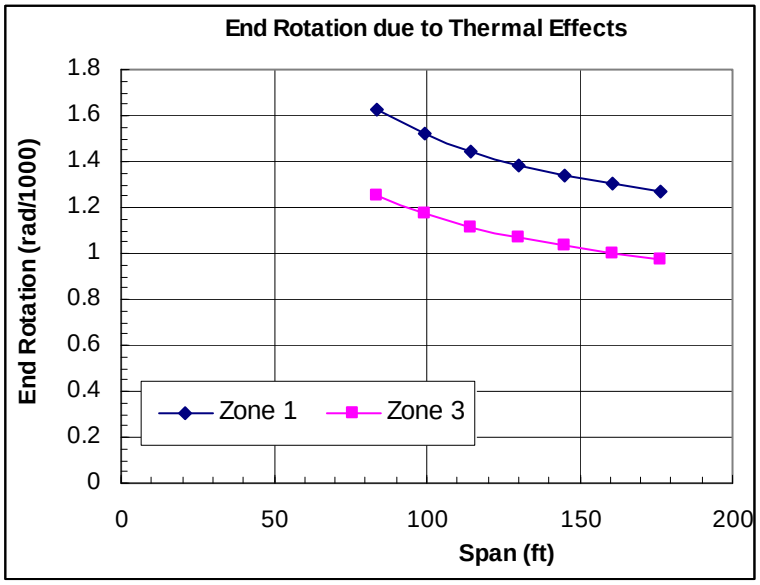

Figure F.39. Rotation due to Thermal Gradient on Girder.

As may be seen, the end rotation is nearly independent of span. This occurs because the end rotation is the product of half span and curvature, and, as the span and depth of the member increase, the thermal curvature decreases and the product changes little. Values are shown for Zone 1 (the most severe) and Zone 3 (the least severe apart from Alaska). Changing the girder spacing from 4ft to 12 ft altered the result by less than ±10%.

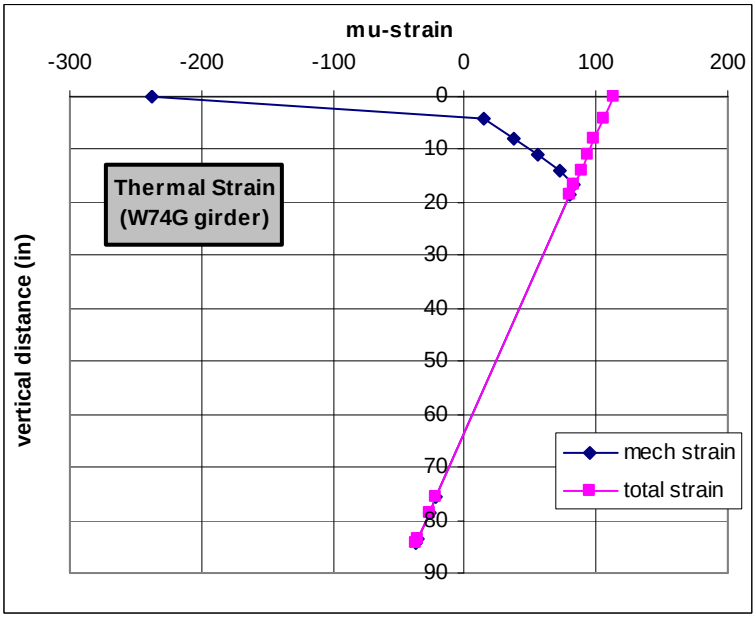

Figure F.40. Strains due to Thermal Gradient.

The variation in strain over the height of the section is shown in Figure F.40, which is drawn for the 74 in. deep girder and the Zone 1 temperature distribution. Both

mechanical strain (stress/E) and total strain (mechanical plus thermal) are shown. Vertical distance is measured down from the top of the slab. Positive strain indicates elongation.

The outcome of these computations is that the thermal camber should be accounted for in design, since it is of the same order of magnitude as the rotation due to live load. Use of a standard value in lieu of detailed calculations might be of interest. A value of 0.0015 radians appears appropriate for that purpose.

F.4 Evaluation of the Design Models

F.4.1 Evaluation Criteria

The test data showed that the debonding is a fatigue behavior, in that the damage accumulates with cycles. However it is somewhat more complicated than fatigue in metals, in which failure eventually occurs by fracture of the part, because in a bearing there is no comparable discrete failure event. The design procedure must take this behavior into account.

The design procedure also needs to take into account cyclic loading from all three potential sources: shear, axial and rotation. The cyclic shear loading typically arises from thermal expansion and contraction of the deck, and contains far fewer cycles than do the compression and rotation fatigue components, so it is neglected in this discussion. However, in some structures, particularly those with deep girders, traffic may also cause shear displacements. For example, end rotation of the girder causes longitudinal displacement equal to the product of the rotation and the distance from the neutral axis to the bottom flange. In some steel structures the girders are attached to a transverse cross beam that is supported on a bearing at each end. Passage of truck traffic then causes the cross-beam to bend and induces transverse shear displacements in the bearings. These shear displacements are likely to be small but numerous.

The analysis of demand in Section F.3 shows that the shear strains due to cyclic compression are much larger than those due to rotation, yet no compression fatigue tests were conducted in this study. Thus some model is needed to account for them in design.

One possibility would be to treat all the cyclic shear strains as equally damaging, regardless of their source. Thus, if a cyclic shear strain of 0.60 in the rotation tests caused 55% debonding after 500,000 cycles, then a shear strain of 0.60 caused by cyclic compression should be assumed to cause the same amount of damage after the same number of cycles. This choice would be consistent with the concept that shear strain is the appropriate measure of damage.

Because the bearings tested during the research were not subjected to load combinations that included cyclic axial force, shear and rotation, no physical results are available for calibrating the model under that loading combination. Therefore the design methods were checked against the conditions for a common bearing type that is used in freeway overpasses. This process does not constitute a calibration in the same sense as matching the predictions of the design method to the measured test data, but it does provide a reality check. The number of such bearings in service is large (approximate calculations based on the number of bridges in the country suggest a million or more), but very few

DoTs report problems with extensive debonding. Therefore the loading on such bearings represents a combination for which the design method should predict no debonding after millions of cycles. Such a check is desirable, because the test data could not be carried out to a number of cycles that represents field conditions. The dimensions and loading for a typical bearing of this sort are given in Design Example 1, in Section 3.2 of this report.

F.4.2 Linear Model

The fit between the cyclic test data and the predictions of the Linear Model is shown in Figure F.18 and Figure F.20. The data contains a lot of scatter, as shown by the R^2 values, but this is to be expected when dealing with fatigue data. However, the model clearly replicates the major characteristics of the data, which are that a larger effective strain leads to a shorter fatigue life for a given level of debonding (25% and 50% in the two figures), and that a reduction in the acceptable level of debonding also leads to a shorter fatigue life. Furthermore, both characteristics are in accordance with expectations of physical behavior.

As a check against common field conditions, the effective strain in a bearing for a typical freeway overpass was computed, and is shown in Figure F.18 and Figure F.20 as an open circle at 50 million cycles. The bearing dimensions and loading are those used in Design Example 1 in Section 3.2. The point lies well below the lines in the figures that represent 25% and 50% debonding. The model therefore predicts a very low level of debonding in such a bearing, and this is in keeping with the low level of debonding in the field implied by the lack of reported problems.

The model has other advantages for the user: it is transparent, it has the same form as the model used by the European Specification EN 1337, and it is simple. It is expressed in Code language in Appendix G. Defining it requires many fewer equations than are needed by the existing AASHTO Method B.

F.4.3 Nonlinear Model

Figure F.22 through Figure F.27 show the fit of the Nonlinear Model defined by Equations (F-67) through (F-73) with the debonding data from the rotation tests. The data show considerable scatter but the Nonlinear Model provides a good fit to the average of the data throughout the entire load history. Fitting the debonding throughout the entire load history is more challenging than doing so only at the end, as was done for the Linear Model, and necessitates a cyclic load factor, c_N, that is a function of the number of cycles and a total strain capacity that is a function of the level of debonding.

The Nonlinear Model was also checked against the typical freeway overpass bearing of Design Example 1. The results are shown in Figure F.41. The vertical scale represents the level of debonding, D, at N cycles. The curve for "fac = 1" is based on using the cyclic shear strain caused by the full live load axial force, plus the full rotation demand of 0.002 radians on the 3-layer bearing. It predicts approximately 70% debonding after 1 million cycles. Many bearings of approximately these proportions exist in the field, and DoTs are not reporting debonding on anything like this scale. Therefore the model is in

some way inappropriate. However, it was very successful in predicting the damage due to rotations in cyclic tests covering a wide variety of variables.

A possible explanation for the failure to predict correctly the response of field bearings lies in the fact that the same shear strain, caused by axial force or rotation, does not in fact lead to the same level of debonding. To investigate this possibility, other curves were prepared, as shown in Figure F.41. They are based on counting only a certain fraction ("fac" in the figure legend) of the shear strain due to axial load in the total cyclic shear strain. The curve for "fac = 0" corresponds to the effect of rotation alone in the cyclic total, and shows no damage at all. While this is in agreement with field experience on bearings of this common size and loading, it is surprising to find that cyclic axial stress causes shear strains that are much larger than those caused by the cyclic rotation, yet they appear to not count towards the fatigue demand on the bearing.

A second possibility is that the model is fatally flawed. However, it was arrived at after considering, calibrating and rejecting five earlier versions, its form has a rational basis that allows it to behave in accordance with expectations at extremes of loading or cycle counts (its form was developed with that specific goal in mind) and it fits the rotation test data remarkably well, including a wide variety of tests with cycle counts from 4000 to 2.2 million. An effort was therefore made to adjust the parameters so as to bring its predictions into line with the very low damage expected in the field bearing described above. The changes required to do so caused its predictions for all of the test data to be completely unrealistic. It is therefore concluded that the fault lies not with the model's ability to represent debonding due to cyclic rotation loading, but rather with the assumed equivalence between cyclic rotation and axial loading.

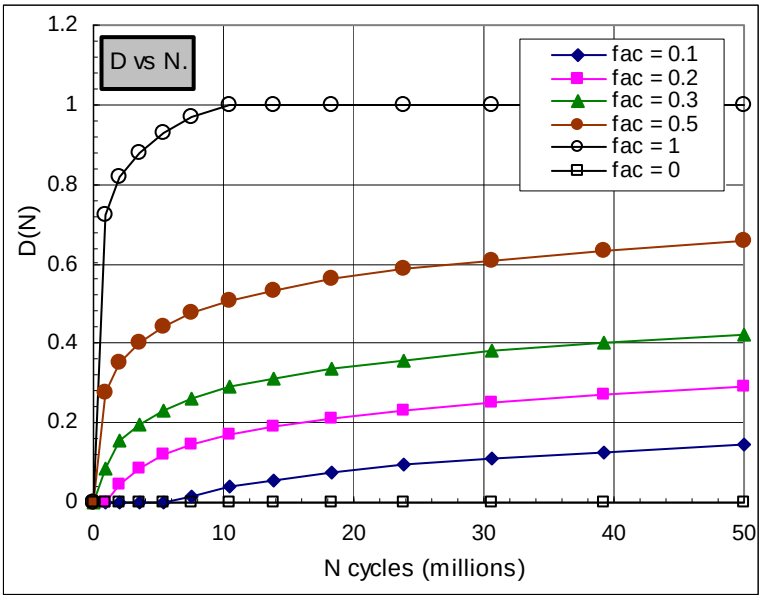

Figure F.41. Predicted Debonding for Example Bearing.

In an effort to investigate the problem further, data from previous compression fatigue testing was sought and analyzed using the Nonlinear model developed here. Compression fatigue tests are reported in NCHRP Report 298 (dated October 1987).

Equations (F-67) through (F-73) were used to predict the amount of debonding in those tests. The test conditions differed from those of the present series, so the results cannot be expected to agree perfectly. The most important differences are:

- The NCHRP 289 test bearings had no edge cover. They were cut from large sheets using a band saw, so the edges were somewhat rough, which may have influenced the start of debonding.

- The material properties were inevitably different to those used in this study, because the testing was conducted approximately 20 years ago. Several different materials were used, for which only the durometer readings, the tensile strength and elongation at break were available. In particular, G and K were not available. The Shore A hardness varied among specimens from 51 to 65. Most were 52 hardness Neoprene, so were at least comparable, if not identical, to those used in the present study.

- The NCHRP 298 specimens were 8" x 8" square, with two rubber layers and S = 5 in most cases. Those used here were rectangular, 22" x 9" with three rubber layers and S = 6 in most cases.

- The loading speeds were different. The previous tests used 1Hz, whereas the present tests were run more slowly, at frequencies on the order of 0.3 Hz.

- The method for measuring debonding was quite different. In the NCHRP 298 study, the rubber eventually started protruding from between the steel shims, due to shear delamination at the shim surface. In the present study, such a measure was not possible because of the cover, so the length of tension debonding along the shim edge was measured, and expressed as a proportion of the total length of the long sides of the two central shims. Thus the previous data measured propagation of shear delamination, whereas the present study measured initiation of tension debonding.

Despite these differences, the NCHRP data were analyzed using the proposed method to predict the debonding after the number of cycles reported from the tests, which varied from about 500,000 to 2,000,000. The material property G from the tests was back-calculated from the stress and strain ranges reported. The results of that process were plausible (e.g. $G \approx 110$ and 200 psi for 52 and 65 durometer material respectively). K was assumed to be 460,000 psi. The test loads were applied as a mean stress, on which was superimposed a cyclic stress range. In the Nonlinear Model, the minimum stress (i.e. the mean minus half the stress range) from the tests was taken as the constant dead load stress, and the stress range from the tests was taken as the live load stress.

This procedure led to the prediction of 100% tension debonding in all specimens but one, where 70% debonding was predicted. The calculations were then repeated, with a scale factor applied to the shear stress caused by cyclic compression. The reasoning for so doing is associated with Fracture Mechanics. If the two types of deformation are associated with different fracture properties, then their propensities for initiation and propagation of debonding might differ, even if the loadings caused the same nominal

shear strain. The results with a factor of 0.5 are shown in Figure F.42. All the cyclic compression test data from NCHRP 298 are shown except the small bearings (4.8" x 4.8"). They had a smaller shape factor than the others, and the results were anomalous, so they were omitted from the comparison.

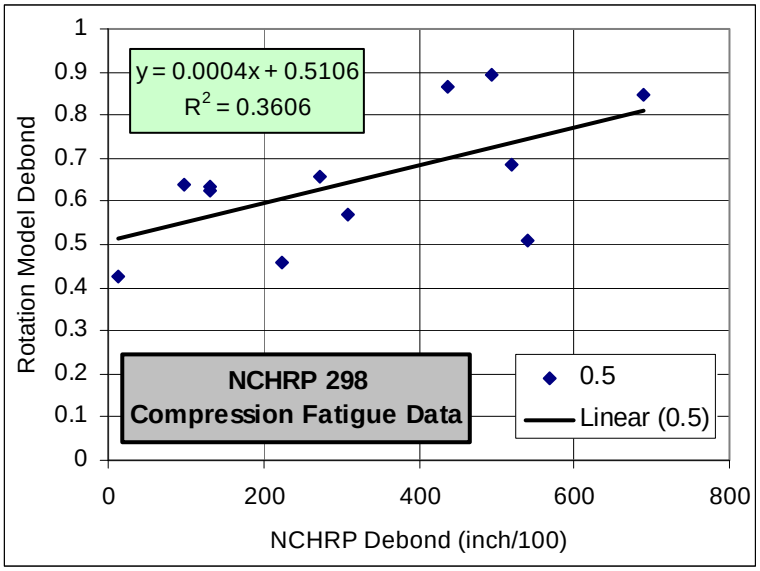

Figure F.42. Compression Fatigue: Predicted vs. Observed Debonding.

The results show a general trend of agreement, inasmuch as both the measured and predicted measures of debonding increase together. There is still considerable scatter, although this should not be surprising in view of the differences between the two approaches and the fatigue loading. These results lend credibility to the Nonlinear Model's general ability to describe the progression of damage under fatigue loading, but the differences between the conditions are too great to permit a numerical calibration. The primary problem lies with the lack of cover in the compression fatigue tests, whereas the model was developed to predict tension debonding between the cover and the edge of the shim.

This finding leads to a difficulty in using the Nonlinear Model for preparing rational design provisions for bearings. The model predicts well the damage due to rotation seen in the tests, but, if the same cyclic amplification factor is used for shear strains due to axial load and rotation, the model predicts debonding in typical freeway overpass bearings that is much more extensive than expected from the lack of damage reported in the field.

F.4.4 Evaluation Conclusions

Two models were developed to relate debonding to cyclic load. The Nonlinear Model provides a more detailed fit with the rotation test data, but it leads to implausible results when applied to common field bearings because, when used with apparently reasonable assumptions about the equivalence between axial load and rotation, it significantly over-estimates the debonding damage caused by cyclic axial loading. The Linear Model is simpler and does provide reasonable predictions for the common field bearings, but was

fitted to the test data only at specific levels of debonding, rather than throughout the entire load history. More refined fitting is not possible because the cyclic amplification factor used in the model is not a function of the number of cycles. Therein lies part of its greater simplicity.

One possible approach would be to implement the Nonlinear Model, and use it to predict the permissible rotation in terms of the desired fatigue life and acceptable debonding level, but to ignore completely the effects of cyclic compression. This would provide better agreement with existing field data, which suggest that failures among elastomeric bearings are very few, but it would be irrational in that the cyclic shear strains due to compression would be ignored, despite the fact that they are much larger than those due to rotation. It seems unlikely that the rubber at the tip of the debonding crack knows whether the shear strain that is driving it arises from cyclic compression or cyclic rotation.

The second possibility would be to implement the Linear Model. It is believed that at this time the Linear Model represents the preferable approach, because of its simplicity and the fact that it both fits the test data and provides plausible predictions for bearings commonly used for freeway overpasses. The latter characteristic represents a useful reality check because the tests could not be carried out to the approximately 50 million cycles expected in the bearing's lifetime.

The most serious problem facing bearing designers today is that the present specifications prohibit both uplift and lift-off, and this creates difficulties with combinations of light compressive load and large rotations. It is proposed here that lift-off be allowed. This solves the problem, provided that the combined shear strains on the compression side of the bearing are not excessive.

Two arguments support this approach. First, permitting lift-off avoids tension stresses in the bearing. It is also shown in Section F.1.2 that, even under lift-off conditions, the total shear strain on the compressive side of the bearing due to combined rotation and axial load may be conservatively estimated computed using the simpler, "no lift-off" equations. This means that the geometrically complicated conditions caused by lift-off can in fact be addressed safely by using a simple computational approach. Second, the results of the monotonic rotation tests PMI-2 through PMI-5 showed that, even with quite large axial loads combined with monotonic rotation, debonding never initiated until a rotation of at least 0.05 radians, and even then it occurred in the A1 bearings which had sharp corners on the shims. The lowest value for other bearings was 0.06 radians. The debonding that occurred did so as a result of large shear strains on the compression side of the bearing. It can therefore be concluded that construction conditions, in which light axial stresses (much smaller than even the 2.5 *GS* used in test PMI-2) are combined with a maximum plausible rotation of 0.04 radians and shims without machined sharp edges, will not lead to debonding.

Thus a strong case exists for permitting lift-off (i.e. allowing separation of the girder from the bearing). For bearings with bonded external plates, lift-off is not possible, and uplift may occur that causes internal tension. For those conditions, a need exists for provisions that will prevent internal rupture in the rubber due to hydrostatic tension. The equations

described in Section F.1.1.5 provide the necessary safeguards against such hydrostatic tension.

F.5 Detailed Development of Specification Provisions

In this section, provisions suitable for inclusion in the AASHTO Specifications are developed, based on the total strain concept embodied in the Linear Model. The Nonlinear Model is not developed to form design provisions.

For consistency with the existing provisions, two design methods are developed. Method B is general and accounts explicitly for axial load, rotation and shear. It is versatile, and may be used to design any bearing. It is developed first. Method A is intended for simple conditions, and represents a special case of Method B, for which assumptions have been made about the rotations so that they do not need to be included explicitly in the design. It is developed from Method B.

F.5.1 Method B

The design criteria for Method B consist of several limits. The first is that the applied shear deformation should not cause a shear strain greater than 0.50. This requirement has been in the AASHTO Specifications for many years, and no evidence arose from this research that suggests that the requirement should be changed. Thus

$$\Delta_s \le 0.5 h_{rt} \tag{F-79}$$

Second, the total shear strain due to axial, rotation and shear effects should be limited. An amplification factor of 2.0 is applied to the cyclic components of the shear strain, as discussed in Section F.2.1. This leads to

$$\left(\gamma_{a,st} + \gamma_{r,st} + \gamma_{s,st}\right) + 2\left(\gamma_{a,cy} + \gamma_{r,cy} + \gamma_{s,cy}\right) \le \gamma_{cap} \tag{F-80}$$

The total shear strain limit is taken as γ_{cap} = 5.0, on the basis of Figure F.18. In that figure, the projected line from the testing reaches 50 million cycles at an effective strain of about 4.7. It was argued that, because some tests never debonded at all, their influence is missing from the figure, so the line should be raised a little to reflect it. For that reason the estimated strain capacity value of 4.7 is rounded up to 5.0. This value is also the same as used in the present European Specification (EN 1337) the previous British Specification (BS5400) and the earlier French Railroad Specification (UIC772R). In the latter case the limit was on shear stress rather than strain, but since stress was assumed to be related linearly to strain, the effect is the same. In EN 1337, the cyclic strains are multiplied by a cyclic factor of 1.0 or 1.5, to be chosen by the owner. Thus the requirements proposed here are more conservative than those specifications. However, the test program on which the present proposals are based was much more extensive.

In addition to the cyclic amplification factor and the total strain capacity, methods of calculating the shear strains from the loading parameters are needed. The shear strain coefficients in Figure F.5 through Figure F.8 were prepared using the equations in Section F.1.1.3.

For bearings without external plates, lift-off is free to occur, and there is no need to check for hydrostatic tension. If external plates exist, then the hydrostatic tension should be evaluated using Equation (F-46). Gent and Lindley's (1959b) experiments showed that rupture occurred when the hydrostatic tension reached approximately 0.9*E*. It is proposed here to use 0.75*E* or 2.25*G*, and to include the amplification factor on the cyclic components of the load, in order to include a margin of safety. It is likely that the cyclic load factor will have little effect in practice, because the critical loadcase for hydrostatic tension is expected to arise during construction, when large rotation angles (due to camber) may accompany light axial loads (due to the girder self weight alone). That loadcase is monotonic.

The following requirements address the possibility of hydrostatic tension due to uplift. In them, the sign of ε_a, and therefore of α, have been reversed so that compressive strain in the elastomer is positive, for consistency with the sign convention presently used in the AASHTO Specifications. The rotation per layer is also designated as θ_i rather than θ_L for the same reason.

"To prevent internal rupture of the elastomer by hydrostatic tension stress, in bearings with externally bonded steel plates, the computed hydrostatic stress shall satisfy:

$$\sigma_{hyd} \le 2.25G \tag{F-81}$$

where σ_{hyd} is the peak hydrostatic tension, computed by

$$\frac{\sigma_{hyd}}{3G} = S^3 \theta_i f(\alpha) \tag{F-82}$$

$$f(\alpha) = \frac{4}{3}\left\{\left(\alpha^2 + \frac{1}{3}\right)^{1.5} + \alpha\left(1 - \alpha^2\right)\right\} \tag{F-83}$$

and

$$\alpha = \frac{\varepsilon_a}{S\theta_i} \tag{F-84}$$

The average axial strain, ε_a, is given by

$$\varepsilon_a = \frac{\sigma_a}{3B_a G S^2} \tag{F-85}$$

and shall be taken as positive for compression in Equation (F-84). Constant B_a is given by Equation (F-19).

For values of α greater than 1/3, the hydrostatic stress is compressive throughout the bearing, and no limit is required. The values of ε_a and θ_i used in Equation (F-84) shall consist of the static components plus 2.0 times the cyclic components".

Other requirements presently in the AASHTO Specifications, such as those for stability and seismic conditions, remain unchanged.

F.5.2 Method A

Method B, as described above, is operationally simpler than the version in the existing AASHTO Specifications. If it is programmed into a spreadsheet or other application, design is quick and simple, so the need for an even simpler Method A is questionable. However, such a method is developed here in the interests of providing choice to the AASHTO T-2 Committee.

The proposed Method A is similar to the existing one, in the sense that it allows the designer to select a bearing on the basis of compressive stress alone. To do this, an implicit allowance for rotation must be made, and it must be large enough to accommodate all rotations that have a reasonable probability of occurrence. Furthermore, to the greatest extent possible, it should allow engineers to continue their present practice of designing common bearings by Method A. However, it should, if possible, also be consistent with the proposed Method B in such matters as using amplified cyclic loads and a definition for the shape factor that is based on the shim size plus half the cover.

Ideally, a bearing that fails to meet the requirements of Method B should not be allowed under Method A, as can sometimes happen under the present provisions. However, this cannot be ensured without some restrictions on the use of the method. The problem is that a bearing with a high shape factor that is subjected to a large rotation will fail to meet the requirements of Method B because of the large rotation, regardless of the axial stress. Because Method A ignores rotation, the bearing could prove satisfactory under it, thereby creating an inconsistency

In order to develop a rational Method A that accounts for these matters, interaction diagrams between normalized axial stress, σ_a/GS, and rotation were prepared, using Method B criteria. These were then used to determine the allowable axial stress that could be carried at the same time as the design rotation. The design rotation should represent the largest feasible rotation demand on bearing.

An example interaction diagram is shown in Figure F.43, for a 9 in. x 22 in. bearing, with 3 layers of ½ in. each. (It is based on G = 110 psi, but variations in G make almost no difference to the result, because the stress is normalized by GS). The two curves represent conditions with maximum shear deformation due to shear displacement and with no shear deformation. The total shear strain capacity is 5.0, as discussed in Section F.5.1 for Method B. The figure shows the combinations of axial stress/GS and rotation per layer that are permissible under Method B. The axial stress and rotation may contain any combination of static and cyclic components, but the coordinate axes represent the total, including the cyclic amplification factor.

The figure also shows a vertical line at the minimum rotation angle for which the bearing should be designed. Within the range of rotation shown, the stress is controlled by the requirement that the axial load must cause a shear strain no greater than 3.0. This leads to an allowable stress of 2.15GS, regardless of simultaneous shear deformations. Constraints related to rotation are therefore not active at the design rotation. Continued

use of the present Method A limit of 1.0 *GS* thus seems very feasible. However, the result is sensitive to the shape factor, the aspect ratio and the number of layers, because these strongly affect the shear strain due to rotation. Those parameters are explored next.

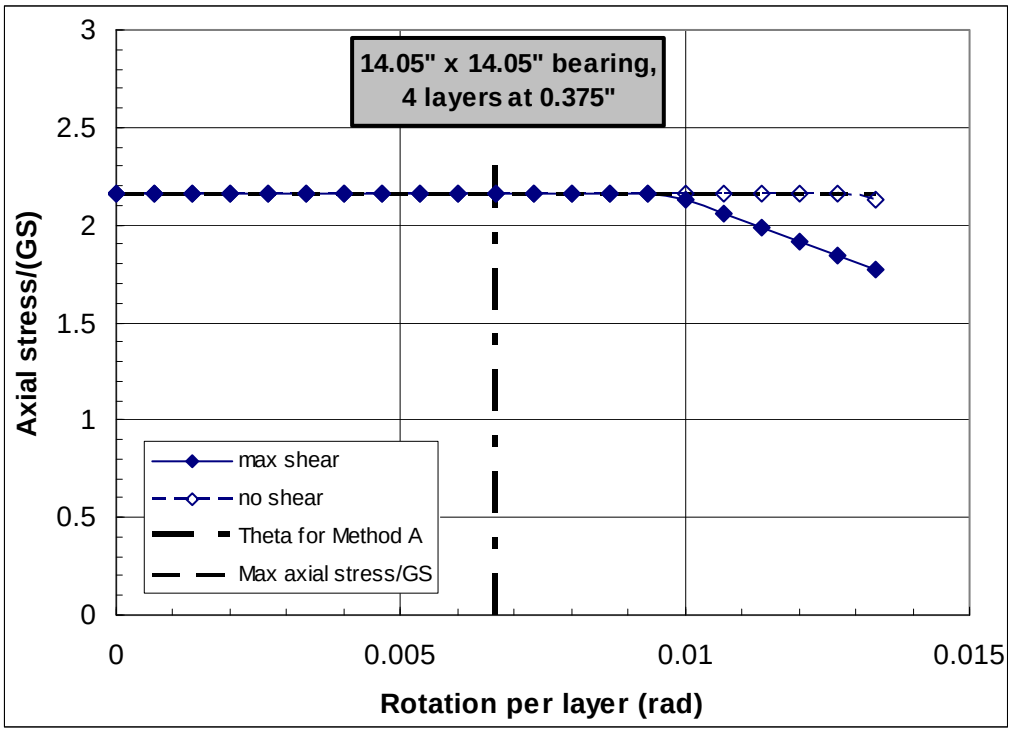

Figure F.43. Axial Stress – Rotation Interaction Diagram. 9" x 22" Bearing, 4 Layers at 0.5".

To illustrate this point, Figure F.44 shows the interaction diagram for a bearing that has the same effective area (190.3 in^2) and the same layer thickness (0.5in.), but is square (14.05" x 14.05"). The change in aspect ratio changes the shape factor slightly, from 6.24 to 6.90. Now the allowable axial stress is a function of the rotation over at least part of the range, and in particular at the design rotation. The shear deformation also reduces the allowable stress. At the design rotation (0.0067 radians per layer in this case) the allowable axial stress is 2.26 *GS* with shear and 1.85 *GS*, without. The existing limit of 1.0 *GS* is still safe, but with less spare capacity than before. The reason is that the square bearing is less able to accommodate the rotations, so less of its total capacity is available for resisting axial load.

To demonstrate the effect of thinner layers and a higher shape factor, Figure F.45 shows the same bearing but with the layer thickness reduced to 3/8". To keep the same total rubber thickness, four layers are used. The normalized stress, σ_d/GS, drops again to 1.30 and 1.70 with and without shear deformations. The shape factor increases thanks to the thinner layers, which partly compensates for the lower normalized stress, but the absolute allowable stress still decreases. A normalized stress of 1.0 *GS* is still feasible.

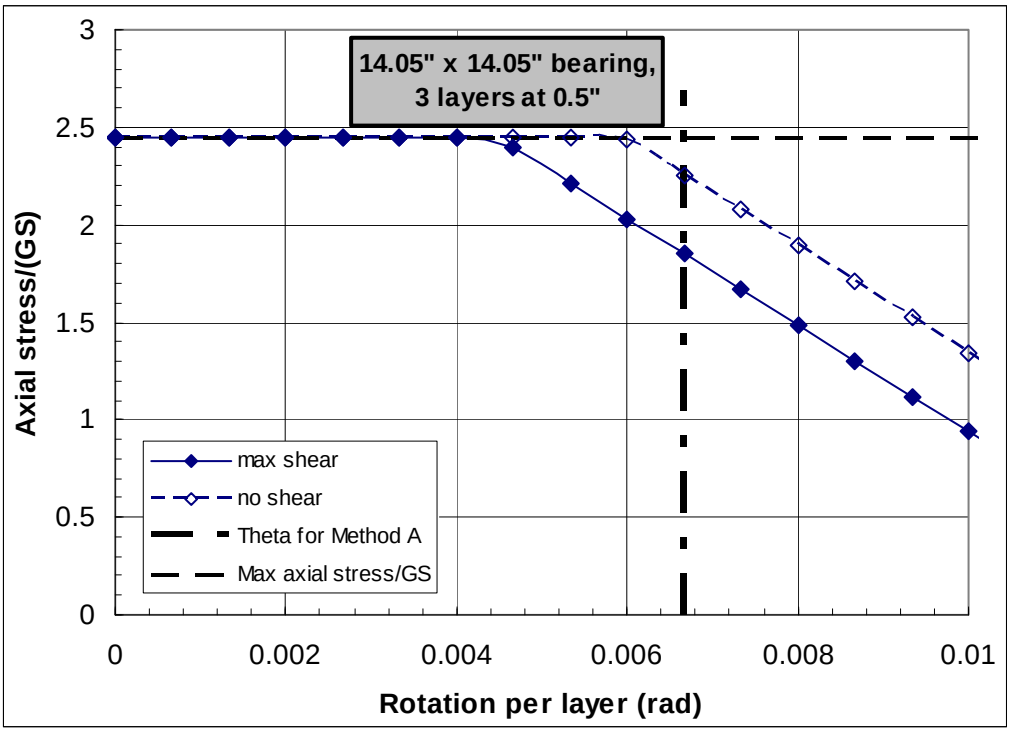

Figure F.44. Axial Stress – Rotation Interaction Diagram. 14.05" x 14.05" Bearing, 3 Layers at 0.5".

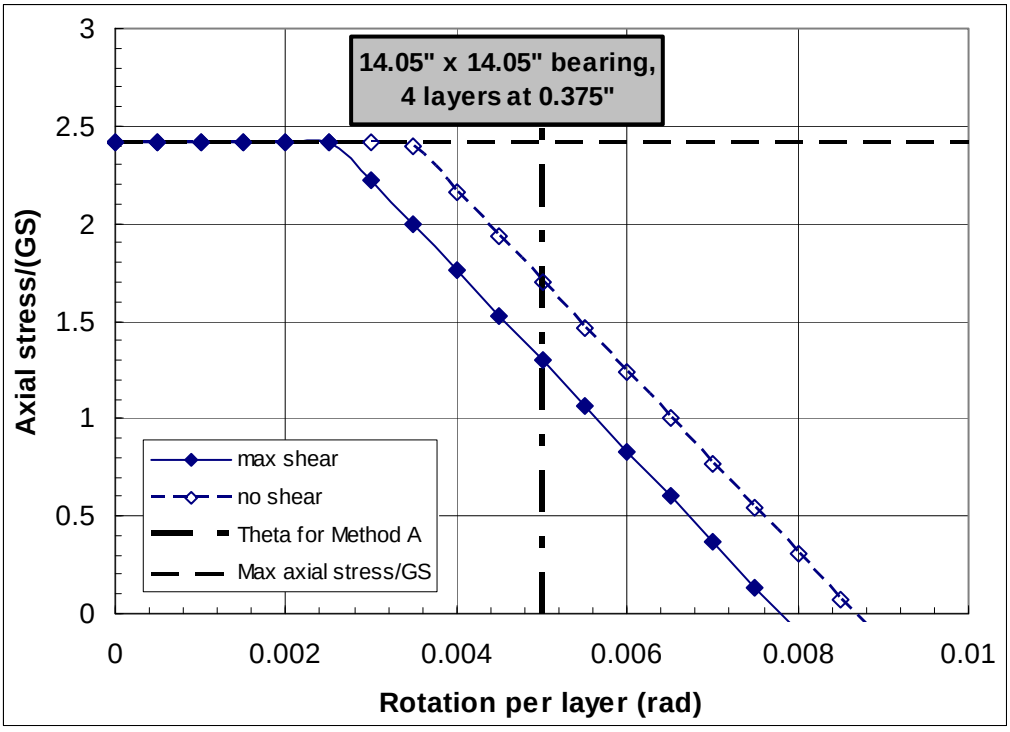

Figure F.45. Axial Stress – Rotation Interaction Diagram. 14.05" x 14.05", 4 Layers at 0.375".

The foregoing arguments show that the allowable axial stress is a function of bearing shape and shape factor and number of layers. Several approaches therefore appear feasible:

- Use an allowable axial stress that is low enough to accommodate all likely shape factors and numbers of layers.
- Use an equation for allowable stress that is a function of shape factor and number of layers.
- Use a fixed allowable stress, but limit the circumstances under which Method A may be used.

The first option was ruled out because the allowable stress would have to be substantially lower than the one in the present Method A. The second option represents essentially what is done in Method B, so there seemed to be little purpose in duplicating it. Thus the third option was adopted here.

The use of Method A was therefore chosen to be contingent on some restriction related to shape factor, number of layers, and applied rotation. Manipulation of the Method B equations shows that the quotient S^2/n, where n is the number of internal layers, provides a suitable control. This is illustrated in Figure F.46, which shows the maximum possible stress at the design rotation as a function of S^2/n. As S increases, or as n diminishes, the quotient S^2/n increases. Then, the shear strains caused by rotation increase, leaving less of the capacity available for resisting axial load.

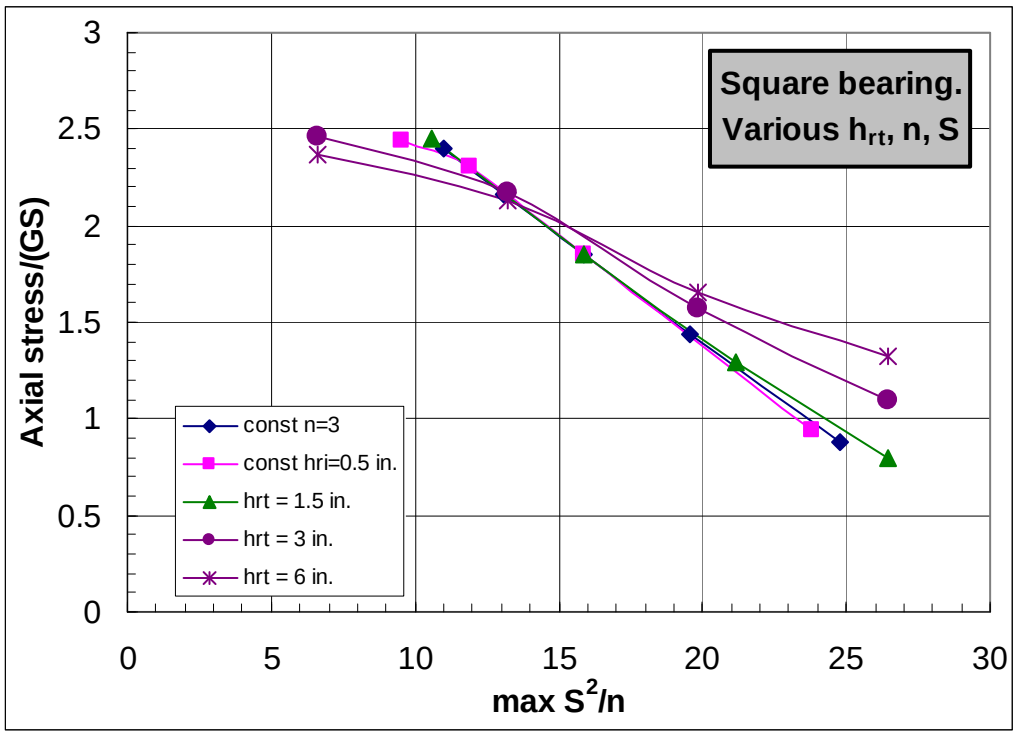

Figure F.46 Allowable normalized axial stress as a function of S^2/n.

Curves are shown for: a constant number of layers (n = 3) but different layer thicknesses; a constant layer thickness (h_{ri} = 0.5in.) but different numbers of layers; and three different total rubber thicknesses (1.5, 3 and 6 in.), for which both the layer thickness and number of layers were changed in such a way as to keep the total rubber thickness constant. If the curves for the two thicker bearings are ignored, the data lie essentially on a single line, suggesting that the term S^2/n is a valid one for limiting the use of Method A.

The value of S^2/n remains to be selected as the limit for use of Method A. Figure F.47 was prepared to help make the decision. It shows the absolute axial stress as a function of S^2/n, for various numbers of layers, n, and was derived by fitting a straight line to the data from the first three curves in Figure F.46. Because the data in Figure F.46 are also subject to the limit of axial stress < 2.4 GS, imposed by the limit on shear strain due to axial load alone, the data for of S^2/n less than about 10 should be ignored. Figure F.47 shows that the allowable stress rises and then falls, with a peak in the middle. This can be explained physically. At very low S, the axial stress capacity is severely limited by the low shape factor, because even a modest axial stress creates very large shear strains. At high S^2/n, the rotation cause high shear strains, leaving little remaining capacity for carrying axial load. The peak in the central region represents a balanced design in which axial load and rotation each causes some shear strain, but neither completely dominates. The peak occurs at an $S^2/n \approx 11$.

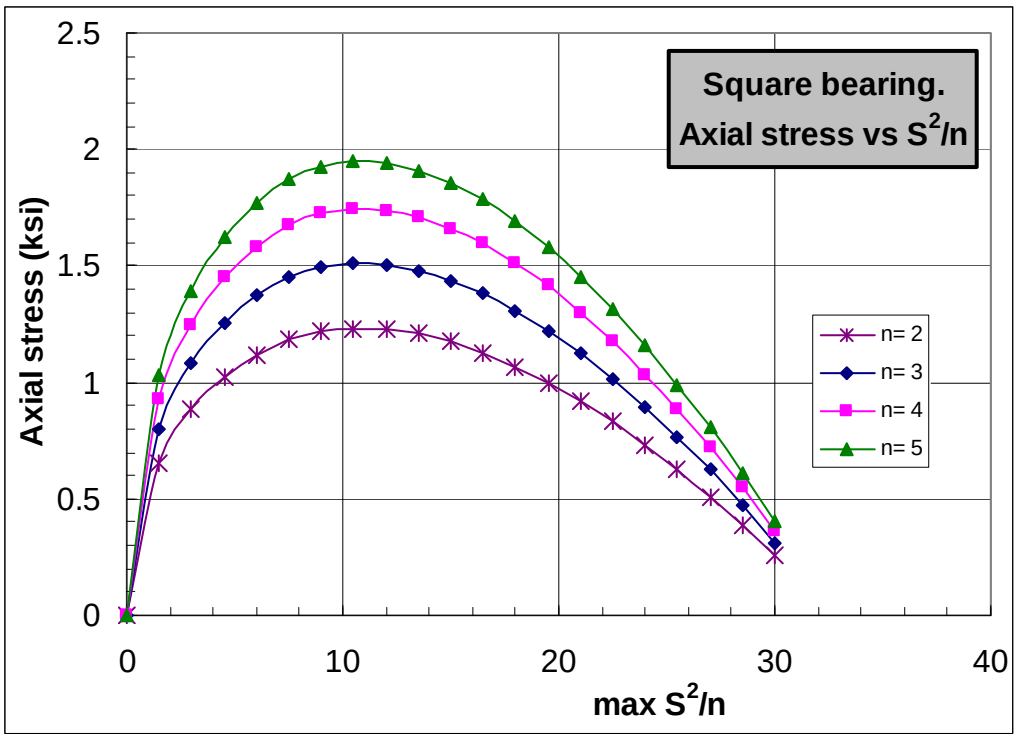

Figure F.47 Allowable axial stress as a function of S^2/n.

This result suggests that $S^2/n \leq 11$ would be an appropriate limit for a Method A design procedure that effectively ignores rotation. If axial stress were the only consideration,

this would indeed be true. For a given number of layers, S will be bounded by the limit $S^2/n \leq c_S$, where c_S is the chosen limiting value of S^2/n, e.g. 11. However, bearing designers tend to use standard layer thicknesses, and manufacturers also favor them in the interests of simplicity. If the layer thickness is also pre-selected, a given S leads to a unique bearing size. Thus the stress (as shown in Figure F.47) and the plan area of the bearing are both limited, so the axial capacity of the bearing, which is the product of the two, is also limited. Results for four example n and h_{ri} values are shown in Figure F.48. The allowable axial load in all cases peaks at $S^2/n < 20$. (This was found to be true for any n or h_{ri}). Thus, even though the highest stress is achieved by using $c_S = 11$, the highest axial load on the bearing can be achieved with $c_S = 20$. This is true because the higher c_S limit leads to a larger bearing. Even though the normalized stress, σ_d/GS, is lower, the larger size more than compensates for it, up to $S^2/n = 20$.

In Figure F.48, the load capacity of the bearing increases significantly with the number of layers. This occurs because, for a given S^2/n, larger n leads to a larger S, which, for a given layer thickness, leads to both a larger S and a larger bearing.

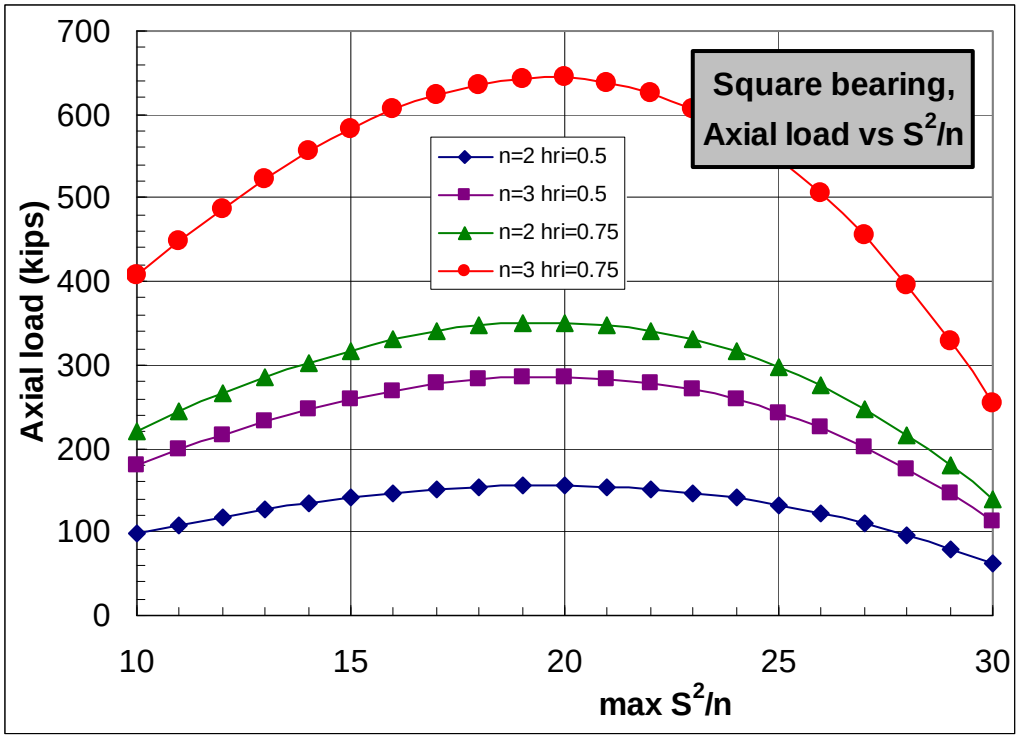

Figure F.48 Allowable axial load as a function of S^2/n

The rational choices for c_S thus lie between 11 and 20. Use of a small value (e.g. 11) would mean that either the number of layers would have to be large, which might be undesirable on the grounds of both economy and available space. Use of a large value (e.g. 20) reduces the stress that can be used, as shown in Figure F.46, but increases the allowable plan dimensions for a given layer thickness. That might also prove not to be

the most economical approach. Consequently, it is proposed here that use of Method A should be permitted only for bearings for which

$$\frac{S^2}{n} \le 16 \qquad \text{(F-86)}$$

This limit of 16 lies in the middle of the plausible range.

To verify that this limit and the corresponding stresses are appropriate, some specific bearings were checked. For example, for the bearing of Figure F.44, which is 14.05 in. by 14.05 in., and has 3 layers each 0.50 in. thick, the quotient S^2/n is 15.9. If the same bearing were constructed using 12 layers of ¼" rubber, S^2/n would still be 15.9 and the normalized allowable stress would also still be 1.85 GS and 2.26 GS with and without shear. (This is very nearly, but not exactly true. The higher shape factor increases λ, which changes the shear strain coefficients D_a and D_r slightly. Apart from that very small difference, the results are identical). However, the absolute allowable stress would be higher in the 12-layer bearing, because S would be higher. Both bearings could accommodate the axial load and rotation.

To illustrate further the effect of aspect ratio, Figure (F.49) shows the effect of keeping the layer thickness and effective plan area the same, but changing the L/W ratio. An L/W ratio greater than 1.0 indicates that rotation is imposed about the strong axis, and vice versa. In all cases the effective plan area was 190.3 in^2 (based on gross dimensions of 9" x 22") and the layer thickness was 0.5".

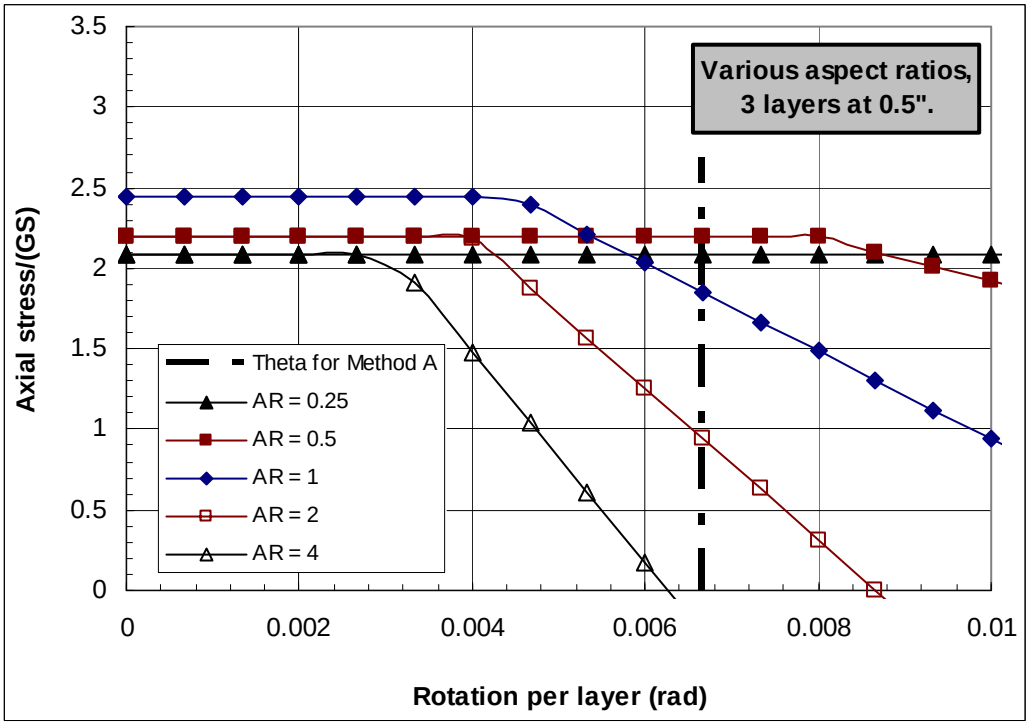

Figure F.49 Interaction Diagram: Effect of Aspect Ratio. (n = 3, h_{ri} = 0.5" for all).

The results show that the rotation effects detract less from the axial load capacity in bearings that are long and narrow, rotated about their weak axes (shown by the lines with solid symbols). By contrast, the reduction in allowable axial stress for a bearing rotated about its strong axis is large. This is not surprising. However, it provides the basis for a second restriction on the use of Method A, namely that rotation should occur about the minor axis of the bearing. This way of expressing the restriction has the virtue of simplicity, but it becomes open to question on bridges with heavy skew angles, in which rotation occurs about both axes. In order to avoid unwieldy rules, it is proposed simply that Method A be permissible if the *primary* rotation occurs about the weak axis of the bearing. In cases of doubt, the designer should use Method B.

The minimum rotation implicit in Method A clearly affects the permissible axial stress, because movement along the horizontal axis of the vertical line representing θ_{min} implies a change in allowable stress. The foregoing calculations used an (amplified) rotation of 0.02 radians. It was made up of

	Radians
Allowance for uncertainty:	0.0100
Thermal camber:	0.0015
Traffic: 2.0*0.004 =	0.0080
Total	0.0195

The 0.0195 was then rounded to 0.02 radians. In each case shown in Figure F.43 through Figure F.49the total rotation of 0.02 radians was then divided by n to give the rotation per layer, θ_L, on the horizontal axis. The S^2/n values in Figure F-49 are 9.98, 14.04 and 15.86 for aspect ratios 0.25, 0.50 and 1.0 respectively.

The rotation of 0.02 radians is relatively conservative, but this is appropriate for a design method that is intended to be simple and ignores rotation. In particular, the allowance for uncertainty, which is given as 0.005 radians in the present AASHTO Specifications, is taken as 0.01 radians here. The reason is that, first, 0.005 radians is a very small angle, and it is not clear that it will be achieved on a regular basis on site. To give an idea of its magnitude, it corresponds to a movement from center of about one tenth of the bubble length in a carpenter's level. Second, it is likely that smaller bearings, such as might be designed using Method A, will be installed to a lower level of accuracy, simply because the errors in level are harder to see. Third, no check is required for construction conditions, when large girder cambers and correspondingly large rotations might exist, albeit in combination with relatively light axial loads. (See for instance, Design Example 3 in the main body of the report). For these reasons, the foregoing assumptions are regarded as reasonable. The traffic rotation is estimated at its worst-case value of 0.004 radians (Equation (F-78)), as is appropriate if no other control exists on it.

The question of determining a value for the allowable stress remains. In the existing AASHTO Specifications Method A, the stress may not exceed 1.0 *GS* or 1.0 ksi in the presence of shear deformations. However these limits refer to loads and rotations to

which no cyclic amplification factor has been applied. A choice must be made over the use of an amplification factor. If Method A were to be changed to include a cyclic amplification factor, then either all the bearing types allowed under those rules would have to be changed, or the design method for steel-reinforced bearings would be inconsistent with the others. The other possibility would be to not use an amplification factor, but then Method A would be inconsistent with Method B.

The second option is the course of action proposed here, on the basis that it is preferable to maintain consistency within Method A, at the expense of external inconsistency with Method B. Furthermore, no information was gathered during the research program about cyclic behavior of other bearing types that are presently allowed under Method A, so a basis for changing them is lacking. Thus the total shear strain capacity, which in Method B applies to amplified loadings, must be suitably reduced to apply to non-amplified loadings in Method A. This cannot be done exactly, because different bearings experience different ratios of static and cyclic loading. However, bounds can be obtained based on maximum and minimum likely ratios of live to dead load.

The Live Load/Dead Load ratio of a bridge lies between about 0.5 (for medium spans) and 1.0 (for short spans). Recall that the cyclic amplification factor in Method B for cyclic loading is 2.0. Therefore, the axial stress limit for a non amplified load should lie between 2/3 (for a short bridge) and ¾ (for a medium span bridge) of the limiting stress for amplified loading. If the average of these values is taken, the non-amplified stress limit should be 71% of the amplified one. For $S^2/n = 16$, the amplified axial stress limit (in the absence of shear displacements) is $1.85GS$, so the non-amplified equivalent is $0.71^* 1.85GS = 1.31GS$. It varies slightly with G, because that affects the compressibility index, λ. It is therefore taken here as $1.25GS$, which is 25% higher than the present Method A limit. A corresponding 25% increase, to 1.25 ksi, is also proposed in the absolute stress limit.

Last, in order to avoid the complication of hydrostatic tension, Method A should not be permitted for bearings with external plates.

It is possible that external plates may be used as the base for a PTFE slider on top of the bearing. It may then be argued that hydrostatic tension is not possible because the stainless steel plate will lift off from the PTFE if the rotation becomes large, thereby protecting the elastomer. This may be true in some cases, but not all. For example, if a relatively large PTFE slider is used for the purpose of avoiding such lift-off, which might in turn lead to edge loading of the PTFE and possible gouging of the stainless steel, then the desired protection for the elastomer will not be available. Method B should be used for such bearings so that the rotation is accounted for properly.

In summary, Method A consists of limiting the axial stress to the smaller of 1.25 ksi and $1.25\ GS$, with a 10% increase permissible if shear displacements are prevented. However, the method may not be used if one or more of the following is true:

- $S^2/n > 16$
- Primary rotation is about the strong axis.
- External plates are bonded to the bearing.

Many states use a 9" x 22" bearing, with three internal layers of ½" rubber, under prestressed concrete girders. Such a bearing has effective dimensions of 8.75" x 21.75", and S_{eff} = 6.24. It has S^2/n = 13.0, and so may be designed by Method A. If G = 110 psi (about 50 durometer), GS = 687 psi, and this limit, rather than the 1250 psi absolute limit controls. The rated axial capacity of the bearing under Method A would be 131 kips. The rated axial capacity could be increased by adding more layers or using a stiffer elastomer.

To reach the axial stress limit of 1250 psi, and the corresponding largest possible load under Method A of 238 kips, GS must be greater than 1000 psi. For G = 110 psi, S must then be increased to 9.1, for which h_{ri} = 0.343". To still qualify for the Method A design procedure, the number of layers must be increased to $S^2/16$, or 5.16, rounded to 6. The total elastomer thickness is therefore 2.058".

The bearing can therefore be designed for a wide range of conditions using Method A, as is desirable. The Method A design uses slightly more rubber and steel than would be necessary under Method B, but, design under Method A is still perfectly feasible. This result simply demonstrates the fact that methods A and B represent two different points along the curve of design simplicity vs. bearing efficiency. It should not be surprising to find that a more precise design method (Method B) leads to a more efficient product.

F.5.3 Discussion of Methods A and B.

Until recently the AASHTO Specifications linked the use of Method B to additional, more rigorous, testing. That testing costs time and money, so it acted as a disincentive to designers to use Method B. That in turn discouraged the use of high shape factors, because the present Method A is subject to limits of both 1.0 ksi and 1.0GS (in the presence of shear displacements). A high shape factor bearing would be limited by the absolute stress limit of 1.0 ksi and the potential load capacity of the high shape factor could not be realized.

However, the tests conducted for this research showed that bearings with high shape factors behaved exceptionally well and that encouraging their use would be beneficial. The recent elimination of the long term test encourages use of Method B and the proposed removal of the existing absolute stress limits in Method B encourage high shape factors because, under those circumstances, the allowable stress under Method B becomes largely a function of GS. A high S will then lead to a high allowable stress, provided that rotations are not excessive.

The long-term test should not be eliminated lightly. Previously, it was applied to bearings designed using Method B, partly because test data were not available on rotations, in which case some doubts remained over the methodology, and partly because Method B bearings were likely to be large, and manufacturing a large bearing is more difficult than making a small one. For example, maintaining the correct shim spacing may become more difficult as the bearing becomes thicker, if it is achieved simply by monitoring the thickness of the layers as they are placed in the mold. Ensuring the correct temperature distribution throughout the rubber is also more difficult as the bearing's plan dimensions increase, because of the risk of over-curing the outer regions before the middle has cured enough.

The tests conducted for this research program provide a considerable data base of experimental evidence to support the design methodology, so the design issue is of less concern than it was. But the difficulties of curing large bearings are still real, and it is proposed that the more rigorous testing be retained for use with large bearings rather than being dependent on the method by which they are designed. Relating the need for additional testing to the size of the bearing is logical because, according to the existing provisions, a large bearing designed under Method A would not need additional testing, even though it may present considerable manufacturing challenges. That weakness would be rectified by this proposal.

It is proposed that special testing be required for any bearing for which the thickness exceeds 8 inches or the plan area exceeds 1000 in^2. The designer is, of course, at liberty to impose the stricter testing requirements on smaller bearings. The matter of testing is discussed in greater detail in Section 3.3 of the main report.

F.6 Summary and Conclusions

In this Appendix the issues of cyclic shear strain demand and capacity on the bearing have been addressed. Sections F.6.1 through F.6.4 summarize the findings.

F.6.1 Summary and Conclusions on Computation of Cyclic Shear Stress

Bearing behavior is inherently nonlinear, but nonlinear theory is too complex to be acceptable for design. However, the linear theory developed by Gent and Lindley (1959a) provides an approximate approach that is accurate and simple enough to be used in practice. The numerical stiffness and stress coefficients for all bearing aspect ratios developed by Stanton and Lund (2004), based on Gent's theory, provide the necessary numerical support for using the linear theory. The nonlinear Finite Element studies described in Appendix E demonstrated that, at small strains, the errors introduced by using the linear approximations are acceptably small. Exact correlation is not possible because the FEA included cover rubber to simulate the test results, whereas the linear theory ignores it.

Previous editions of the AASHTO Specifications have contained bearing design provisions that prohibit any net upward movement of any point on the bearing relative to its unloaded position. This has been a major source of frustration for designers, who have found that that provision controls when the load is light and the rotation is large, as may occur during construction. It is proposed here that that restriction be eliminated. Doing so necessitates that protection be provided against the possibility of internal rupture through hydrostatic tension, which is mostly likely to occur when external plates are bonded to the bearing. A computational method was developed for determining the hydrostatic tension stress in a bearing that is equipped with bonded external steel plates and that is subjected to light axial load and large rotations. This condition is referred to as "uplift". The calculation method forms part of the proposed specification provisions.

Rupture is unlikely to occur in bearings from which the girder can experience partial lift-off if there is no tension connection between the bearing and the sole plate. In that case

the peak shear strains due to combined compression and rotation can be conservatively predicted using the linear theory while ignoring lift-off. Furthermore, this approximation is likely to be needed only rarely, because lift-off during service loading was shown to be improbable for the magnitude of the service rotations expected in practice.

F.6.2 Summary and Conclusions on Cyclic Shear Stress Capacity

Cyclic shear strain capacity is controlled by debonding of the elastomer from the steel shim plates. Cyclic rotation tests were conducted to investigate the initiation and propagation of debonding, and they are described in Appendices A and D. Those test results were analyzed in this appendix and two models were developed to predict the relationship between applied loading and debonding.

The Nonlinear Model provides a more detailed fit with the test data, because it is able to relate the debonding damage level to the number of cycles. It has a rational form that ensures logical behavior as the various parameters, such as cycle count, tend to extreme values. It is expressed in a form that is suitable for use in design, and was calibrated to fit the test data. The fit was good, despite the wide variety of conditions represented by the test series. However, the resulting equations are quite complicated. Problems also arose because the shear strains caused by cyclic axial loads were found to be much larger than the shear strains due to rotation. During this research, no tests were conducted on cyclic axial load, so suitable data were not available for calibrating the model to account for it. To overcome this difficulty, the assumption was made that the same shear strain, whether caused by axial load or rotation, would contribute equally to debonding damage. However, use of this assumption led to predicted levels of debonding in common bearings used for freeway overpasses that are at odds with field experience. No simple way could be found to overcome this drawback of the method.

The second candidate design method, referred to as the Linear Model, is simpler but cannot be calibrated to the entire load history, because the cyclic amplification factor in it is a constant rather than a function of the number of cycles. However, it fitted the major trends in the data, and it was able to predict very low levels of debonding in the typical field bearings. Such bearings typically display very little or no debonding.

The Linear Model is therefore recommended for implementation at this time. However, the Nonlinear Model is described in full in this appendix so that, when suitable test data on cyclic axial load become available, they may be used to complete the calibration of the model.

F.6.3 Summary and Conclusions on Cyclic Shear Stress Demand

Rotation and axial force demands on the bearing were analyzed by considering truck and lane loading on a bridge. Several parameters were varied to study the range of possible demands.

It was found that the live load rotation demand on the bearing is always less than or equal to 0.004 radians and often less than 0.003 radians, provided that the bridge satisfies the AASHTO requirement that the mid-span deflection is less than $l/800$. In many cases,

particularly when prestressed concrete girders are used, the deflection will be only one half or one third of that permissible value, and the rotation will also be correspondingly smaller. Coefficients were developed to account for continuity, which reduces the end rotation still further. The cyclic shear strains in the elastomer caused by these rotations, for a typical bearing design, are small compared with the elastomer's capacity.

By contrast, the shear strains caused by cyclic axial forces are significantly larger than those caused by cyclic rotations. The ratio can be a factor of 5 or more, particularly if the girders are spaced quite widely. If shear strain in the elastomer is indeed the best metric of debonding damage, then cyclic axial load effects are much more important than rotation for bearing design.

Truck loading causes both axial load and rotation on the bearing. However, each of these two effects reaches its individual maximum when the truck is in a different location on the bridge. Therefore it is necessary to find the truck location that causes the largest combined effect. That value depends to some extent on the geometry of the bearing selected, but, for common bridges (with spans less than about 200 ft), the critical condition occurs when the truck is just entering the bridge, with the rear axle over the bearings. (The values obtained when the truck is just leaving the bridge were found to be only slightly smaller). Unless the conditions are unusual, the combination of rotation angle and axial load that correspond to that truck location will be the critical one.

F.6.4 Summary and Conclusions on Model Evaluation

Two possible design approaches are possible. In the first, the Nonlinear Model could be implemented, with the proviso that the fatigue effects of cyclic shear strain due to axial load effects would be ignored, and it would simply be treated as a static loading. Cyclic shear strain due to rotation would be evaluated according to the model developed from the test results. This would cause the predicted debonding levels to agree with field experience on common bearings, which is dominated by cyclic axial effects, and with the test data, which was dominated by cyclic rotation. However it would be illogical because it would treat the two sources of cyclic shear strains differently.

In the second approach, the Linear Model could be implemented. The restrictions on lift-off in the present specifications would be removed, but new restrictions on uplift would be included to prevent the damage by internal hydrostatic stress that could occur in bearings with external plates.

Because of the relative simplicity of the Linear Model, and the fact that it both fits the test data and provides reasonable predictions for a common class of bearings used in practice, it is recommended for implementation at this time. The proposed Specification provisions in Appendix G are based on it. No specification provisions based on the Nonlinear Model are presented.

The proposed specification provisions contain both design Methods A and B. Method B was built on the Linear Model for strain capacity, and Method A was derived from it. Because Method A ignores rotations, restrictions were developed to prevent it from being used under circumstances when rotation effects are especially important. Those restrictions unavoidably and correctly penalize the use of high shape factors. It is therefore appropriate to encourage the use of Method B, which is not only much simpler

to use than the existing version but also provides an incentive to use higher shape factors where appropriate.

The more rigorous testing requirements that were formerly associated with Method B designs have recently been eliminated by the AASHTO T-2 Committee. In order to guard against failure caused by the difficulties of fabricating large bearings, it is proposed that large bearings should be tested using the more rigorous test procedures that used to be applicable to Method B bearings.